Geophysical and Astrophysical Fluid Dynamics
Vol. 00, No. 00, 00 Month 2012, 1–36

Laboratory observations of a transient turbulent Ekman layer

Max Coppin[a,b], Bruno Deremble*[a], Joel Sommeria[b], Thomas Valran[b], Samuel Viboud[b], Maria Eletta Negretti[b]

[a]Université Grenoble Alpes, CNRS, INRAE, IRD, Grenoble-INP, Institut des Géosciences de l'Environnement, Grenoble, France
[b]Université Grenoble Alpes, CNRS, Grenoble-INP, Laboratoire des Écoulements Géophysiques et Industriels, Grenoble, France

(*June 10, 2026*)

We investigate the transient dynamics of a turbulent Ekman boundary layer through large-scale spin-up experiments on the Coriolis rotating platform in Grenoble. An impulsive change in rotation rate generates a well-controlled bottom stress, exciting inertial oscillations that decay over several inertial periods, more slowly than laminar theory predicts. We show that this behaviour is controlled by the bottom stress formulation: a quadratic drag law $\tau_b = C_f|\mathbf{u}|\mathbf{u}$, with $C_f \approx 5 \times 10^{-3}$, correctly reproduces both the damping rate and the interior spin-up. Despite the slow attenuation, the steady Ekman spiral and the inertial oscillations superpose linearly, extending a result trivially expected in the laminar case to the turbulent regime. The k-ε closure appears to be in good agreement with the data.

Keywords: Turbulent Ekman layer, Inertial oscillations, Spin-up, Bottom drag, k-epsilon model

1. Introduction

Oceanic boundary layers at the surface and seafloor are key sites of energy injection and dissipation (Wunsch and Ferrari 2004). At the surface, wind stress drives a turbulent mixed layer whose depth controls air–sea exchanges of heat, gases, and momentum. At the seafloor, bottom friction dissipates the kinetic energy of geostrophic currents and tidal flows, and sets the bottom boundary condition for the large-scale circulation (Pedlosky 1996, Vallis 2006). Yet, representing these layers in numerical models remains a challenge, as their turbulent structure depends sensitively on the choice of closure scheme and boundary conditions.

Observations of the bottom boundary layer over continental shelves and in the deep ocean have documented the Ekman spiral, the log-layer structure of the mean velocity, and the inhibition of turbulence by stable density stratification (Weatherly and Martin 1978, Perlin et al. 2005, 2007). At the ocean surface, direct current measurements have also confirmed the Ekman spiral and the wind-driven mixed layer deepening (McPhaden et al. 2024, Price et al. 1978). Laboratory experiments have played a complementary role in advancing our understanding of turbulent boundary layers. In particular, the spin-up experiment of Kato and Phillips (1969), in which a stress is applied at the surface of a rotating, stratified fluid, has become a standard benchmark for testing turbulence parameterizations (Price et al. 1986, Umlauf and Burchard 2003).

The dynamical regime in the boundary layer under the influence of constant surface stress has been described in the seminal work of Ekman (1905), who showed that the steady balance between the Coriolis force and the divergence of the vertical momentum flux gives rise to a

*Corresponding author. Email: bruno.deremble@univ-grenoble-alpes.fr

veering spiral confined within a depth $\delta_E = \sqrt{2\nu/f}$, where f denotes the Coriolis parameter and ν the kinematic viscosity.

In geophysical flows, molecular viscosity can be tentatively replaced by a turbulent eddy viscosity $\nu_t \sim u_* \delta_E$ (with u_* a friction velocity), yielding the turbulent scaling $\delta_E \propto u_*/f$ (Rossby and Montgomery 1935, Zilitinkevich and Mironov 1996). Unlike the laminar case, for which the momentum equations are linear and admit an exact analytical solution, turbulence introduces nonlinearities through the Reynolds stress terms, which couple the mean flow to the velocity fluctuations. The eddy viscosity $\nu_t(z,t)$ is no longer a known quantity but must be modeled, giving rise to the turbulence closure problem.

Several modelling approaches have been proposed to better understand this physical situation, as reviewed by Kim et al. (2014): slab models, which ignore the vertical structure entirely (Pollard and Millard 1970, D'Asaro 1985, Alford 2001); imposed eddy-viscosity profiles $\nu_t(z)$, which prescribe the turbulent mixing without a dynamical equation for the turbulent kinetic energy (Faller and Kaylor 1966, Madsen 1977, Endoh and Nitta 1971, Lewis and Belcher 2004). Another approach is to use linear Rayleigh damping $-r\mathbf{u}$, where the empirical coefficient r aggregates unresolved mechanisms such as wave breaking and turbulent dissipation (Csanady and Shaw 1980, Ashkenazy et al. 2015, Kim et al. 2014). In coarse-resolution ocean models, linear or quadratic friction coefficients are typically defined as a bulk drag coefficient relating the bottom stress to the depth-averaged or near-bottom velocity. Whether this bulk value is consistent with the local boundary drag coefficient inferred from the Law of the Wall remains an open question, particularly in the transient regimes where the logarithmic layer may not be fully established. More sophisticated two-equation closures, such as the k-ε model, have been applied to the steady turbulent Ekman layer and shown to agree well with high-resolution DNS (Braun et al. 2020, Marlatt et al. 2012).

The steady turbulent Ekman layer is only part of the picture. Wind stress is inherently unsteady. Impulsive or intermittent forcing excites inertial oscillations which carry a significant fraction of the near-surface kinetic energy and represent a major pathway for momentum transfer into the deep ocean (Pollard and Millard 1970, D'Asaro 1985, Alford 2001). In the linear framework, the transient inertial response and the steady Ekman spiral simply superpose (Pollard and Millard 1970): inertial oscillations produced by the onset of a constant stress decay through frictional dissipation, leaving eventually the steady Ekman balance. In the turbulent regime, however, this decoupling breaks down: the oscillating shear modulates the eddy viscosity $\nu_t(z,t)$, which in turn alters the vertical Ekman spiral profile (Coppin et al. 2025). This two-way coupling is a fundamentally nonlinear effect, and its consequences for the decay rate of inertial oscillations and the structure of the turbulent Ekman layer remain poorly documented.

The open questions that we aim to address in this study are the following: first, the decoupling between inertial oscillations and the Ekman spiral, exact in the laminar case, has not been verified in the turbulent regime. Second, the sensitivity of inertial oscillation decay to the boundary condition remains poorly explored. Third, the ability of turbulent closures to reproduce the transient turbulent Ekman layer has not been assessed against data. We consider the k-ε model (Burchard and Bolding 2001), a two-equation scheme that solves prognostic equations for the turbulent kinetic energy and its dissipation rate, widely used in ocean modelling but has rarely been tested in transient, rotation-dominated regimes.

To address these questions, we present large-scale spin-up experiments conducted on the Coriolis rotating platform in Grenoble (France). The spin-up process has been extensively studied since Greenspan and Howard (1963) (see the review by Duck and Foster (2001)), but few experiments have reached turbulent regimes (Caldwell et al. 1972, Sous et al. 2013), and none have documented the transient oscillating stage that immediately follows the impulsive forcing. The large Reynolds numbers achieved on the Coriolis platform allow the boundary layer to be fully turbulent while preserving a clear inertial signal. We focus on the weakly

stratified limit, for which rotation rather than buoyancy constrains the vertical structure: in strongly stratified regimes the Ekman layer becomes buoyancy-limited to a depth $\delta_E\sqrt{f/N}$ (Pollard et al. 1973, Fernando 1991, Kato and Phillips 1969). The threshold value of f/N at which this transition occurs remains poorly constrained (Zilitinkevich 2012). We investigate the regime $f/N \sim \mathcal{O}(1)$, where rotation rather than buoyancy is expected to control the vertical structure of the flow.

The paper is organized as follows. The experimental setup and measurement techniques are described in Section 2. Section 3 develops the theoretical framework: the 1D axisymmetric model, the friction law, and inertial oscillations together with laminar analytical solutions for the no-slip and free-slip limits. Results are presented in Section 4 and Section 5, where mean flow profiles, turbulent statistics, and the transient inertial response are compared against the k-ε closure. Section 6 summarizes the findings and discusses their implications for the parameterization of oceanic boundary layers.

2. Experimental Methods

To investigate the transient dynamics of a turbulent Ekman layer under controlled conditions, laboratory experiments were carried out in the Coriolis Platform at Grenoble (Fig. 1). The circular tank (13 m in diameter) is filled with water to a depth $H = 0.5$ m. The forcing is produced by an impulsive change in the platform rotation speed, which generates an azimuthal flow in the platform frame of reference. This procedure is referred to as *spin-up* when the rotation speed increases, and *spin-down* when it decreases. The platform reaches its nominal rotation speed after an acceleration phase of 20 s.

Throughout this paper, we use cylindrical coordinates (e_r, e_θ, e_z) when describing the flow in the tank. The vertical coordinate z is oriented upward, with origin $z = 0$ at the tank floor (where the forcing is applied). The three velocity components (u_r, u_θ, u_z) are measured by Stereoscopic Particle Image Velocimetry (S-PIV) in a vertical plane tangent to the azimuthal direction at the fixed radius $r_0 = 4.5$ m.

2.1. *Experimental Configuration*

The experiments are characterized by three main external control parameters: the Coriolis parameter $f = 2\Omega_i$, set by the initial background rotation rate Ω_i of the platform, the impulsive change in rotation speed $\Delta\Omega = \Omega_f - \Omega_i$, and the buoyancy frequency N, set by the initial density stratification.

2.1.1. *Background rotation*

The platform rotates at an initial angular velocity Ω_i, which sets the background rotation of the fluid and defines the Coriolis parameter $f = 2\Omega_i$. In the rotating experiments, $\Omega_i = 0.05\ \mathrm{rad\,s^{-1}}$, corresponding to an inertial period $T_f = 2\pi/f \approx 63$ s. In the non-rotating reference case, $\Omega_i = 0$ and the relevant time scale is instead set by the impulsive forcing $\Delta\Omega$.

2.1.2. *Mechanical Forcing*

The forcing is generated by an impulsive change in the platform rotation rate, which appears as a suddenly imposed bottom velocity in the initial reference frame, while the fluid far above remains at rest temporarily due to inertia. In all the experiments presented here, the same rotation rate increment $\Delta\Omega = 0.05$ rad s^{-1} is applied. At the measurement radius $r_0 = 4.5$ m, it results in a given bottom velocity $v_0 = r_0\,\Delta\Omega = 23.5\ \mathrm{cm\,s^{-1}}$. The resulting bottom stress $\tau = \rho u_*^2$, where u_* is the friction velocity, drives the formation of the Ekman boundary layer and the subsequent spin-up of the fluid column. Due to the veering effect of

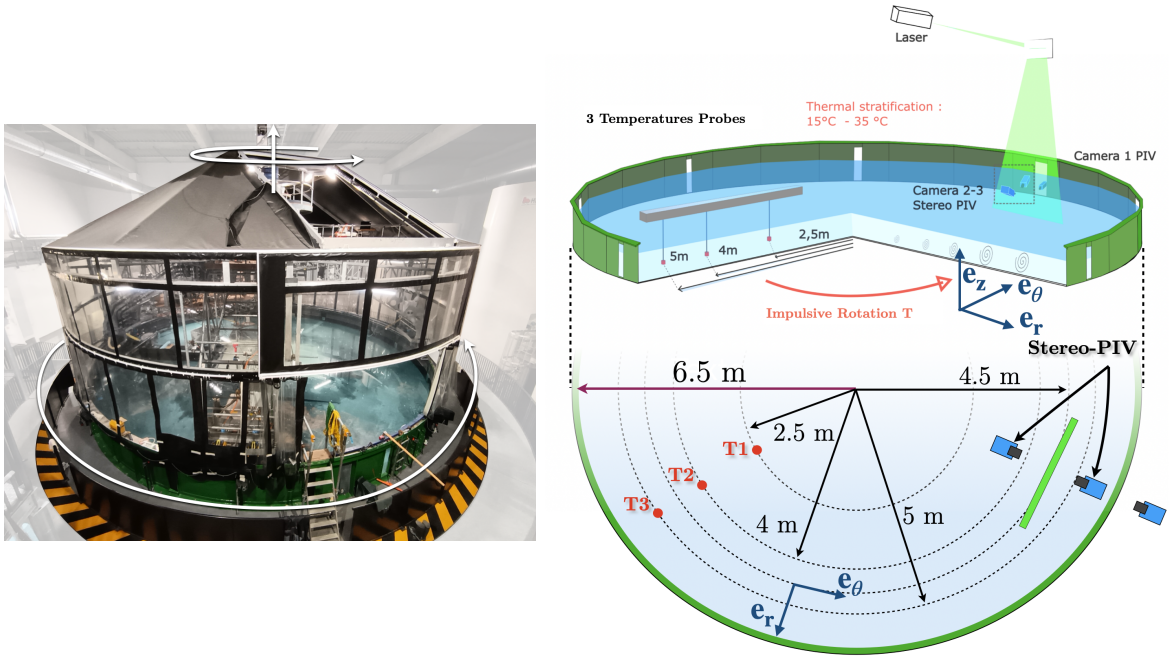

Figure 1. Illustration of the experimental apparatus. Left: Picture of the 13 m wide rotating Coriolis Platform. Right: Schematic side and top view of the experimental set-up. The water height in the tank is 50 cm.

the Coriolis force, the stress is tilted by an angle α_0 with respect to the azimuthal direction, so we must distinguish the azimuthal shear stress $\tau_\theta = \rho u_*^2 \cos\alpha_0$ and the radial shear stress $\tau_r = \rho u_*^2 \sin\alpha_0$.

The friction velocity will be estimated from the measurements of the total vertical flux of azimuthal momentum,

$$\tau_\theta = -\left\langle v'w'\right\rangle\Big|_{z\to 0} + \nu \left.\frac{\partial\langle v\rangle}{\partial z}\right|_{z\to 0}, \tag{1}$$

which remains approximately constant with z in the wall layer. Since the spatial resolution of the S-PIV does not allow us to resolve the viscous sublayer, u_* is estimated by extrapolating the measured momentum flux profile toward the wall. We can similarly estimate the radial stress τ_r from the radial velocity component u. Typical values obtained for the friction velocity are $u_* \simeq 0.8\ \mathrm{cm\,s^{-1}}$ (see section 4.2).

2.1.3. *Density stratification*

We perform experiments with no stratification to study the canonical Ekman layer. Along with these experiments, we consider the weakly stratified limit to provide a comparison with the reference experiment of Kato and Phillips (1969). This stable density stratification is due to a constant vertical temperature gradient established prior to each experiment by filling the tank progressively from the bottom. The injected water is a mixture of water preheated to 40^oC and cold tap water at approximately 17^oC, with the hot fraction decreasing continuously from 100% at the start to 0% at the end of the filling. To avoid turbulent mixing during filling while limiting heat loss to the atmosphere, the tank is filled over 4 h to reach a depth of $H = 50$ cm. The resulting density profile is characterized by the buoyancy frequency N defined by

$$N^2 = -\frac{g}{\rho_0}\frac{\partial\rho}{\partial z} = g\alpha_T \frac{\partial T}{\partial z}, \tag{2}$$

where α_T is the thermal expansion coefficient and ρ_0 a mean reference density. The value of N is approximately uniform over the lower 30 cm of the water column. The upper layer

($\approx$ 20 cm) is mixed due to convection at the water–air interface; we do not consider this upper layer further in the analysis. The stratification obtained with temperature is weaker than those usually obtained with salinity, in order to explore the limit of weak stratification. The choice of a temperature stratification instead of the more usual salt stratification was motivated as part of a wider project involving thermal convection, not discussed here.

2.1.4. *Overview of the experiments*

In this article, we analyse four main experiments defined by the presence or absence of background rotation and stable stratification, as summarized in Table 1.

Label	f (rad s^{-1})	N (s^{-1})
EXP-Ref	0	0
EXP-S	0	0.25
EXP-R	0.104	0
EXP-SR	0.104	0.32

Table 1. Experiment names with values of the control parameters. f is the Coriolis parameter, N the buoyancy frequency. In all the experiments, the water depth is $H = 50$ cm and $\Delta\Omega = 0.05$ rad s^{-1}, corresponding to a bottom velocity $v_0 = 23.5$ cm s^{-1} at the reference radius $r_0 = 4.5$ m, where velocity measurements are made.

2.2. *Measurement techniques*

We use three complementary techniques to observe the flow: laser-induced fluorescence (LIF), which gives a qualitative picture of the flow structure; Stereoscopic PIV (S-PIV), which provides the three velocity components in a vertical plane; and vertically profiling thermistor probes, which resolve the temperature stratification.

2.2.1. *Laser-induced fluorescence*

Figure 2 presents a snapshot of the flow during the transient growth of the boundary layer, visualised using fluorescent dye (rhodamine 6G) injected at the tank floor at the beginning of the experiment. The image is taken in the (e_θ, e_z) plane; the bottom stress drives the flow from left to right. Immediately above the floor lies the *viscous sublayer*, a thin region where viscous stresses dominate and the velocity profile is linear, which is too thin to be visible in the figure. Above it lies the *log layer*, a region where the flow is governed by the law of the wall, with a logarithmic mean velocity profile whose range increases with the Reynolds number.

Above this log layer, the *mixed layer* is characterised by an approximately uniform dye concentration, reflecting efficient scalar mixing by turbulent eddies. The velocity field within this layer, however, retains significant vertical structure: it decreases monotonically with height in the non-rotating case, and adopts an Ekman-like veering profile when background rotation is present. In the rotating case, the Coriolis force confines this active layer to a depth $\delta_E \sim u_*/f$, beyond which the flow decouples from the bottom stress.

At the top of the mixed layer, the *entrainment layer* marks the transition to the quiescent stratified interior above. It is visible in Fig. 2 as the bright, turbulent interface where overturning structures erode the stratification. The entrainment is driven by Kelvin–Helmholtz billows, which arise when the local Richardson number falls below $Ri_c \approx 0.25$ (Miles 1961, Howard 1961). Overturning intrusions and small-scale eddies then engulf pockets of stratified fluid.

2.2.2. *Stereoscopic Particle Image Velocimetry (S-PIV) and image processing*

The velocity field is measured in a vertical plane located at $r_0 = 4.5$ m from the centre (2 m from the outer boundary) using Stereoscopic Particle Image Velocimetry (S-PIV), which provides the three components of the velocity field in a two-dimensional plane. The fluid is seeded with polyamide particles (Orgasol, 60 μm diameter), which are approximately neutrally

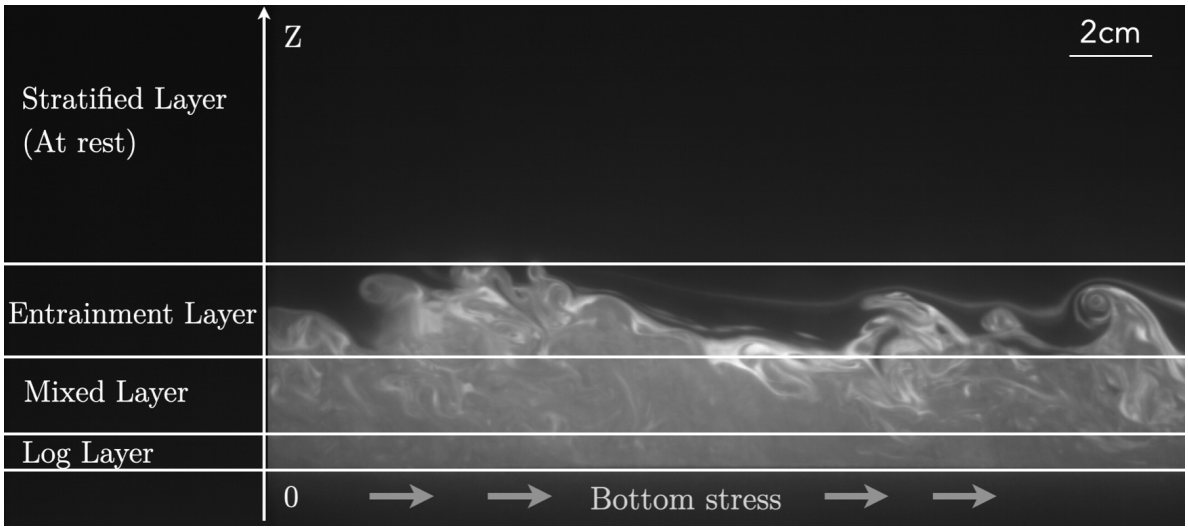

Figure 2. EXP-S: Snapshot of vertical view, at $r = 4.5$ m, of the boundary layer turbulence revealed by a fluorescent dye (in white) injected into the denser water at the bottom prior to the experiment. The horizontal lines qualitatively illustrate the vertical structure of the flow. The black region above is at rest.

buoyant. The particles are illuminated by a continuous 5 W YAG laser source operating at $\lambda = 532$ nm, shaped into a vertical light sheet by a Powell lens. Two cameras (PCO, 2048×2048 pixels, 14-bit monochrome) are mounted on both sides of the light sheet, observing the same plane from two different view angles. Each camera provides the particle displacement in the plane perpendicular to the line of sight, so the three velocity components can be deduced by geometric projection.

Images are acquired in short bursts of 3 frames at 100 Hz, repeated five times per second. All image processing is performed with the UVMAT software. The processed velocity fields have a spatial resolution of 1 mm in both the horizontal (e_θ) and vertical (e_z) directions, and a temporal resolution of 0.2 s. Further details on the S-PIV method are given in Sous et al. (2013).

The view field spans $L_{\text{laser}} = 32$ cm along the azimuth. The cartesian velocity components (u_x, u_y, u_z) in this tangential vertical plane can be treated as the cylindrical components (u_θ, u_z, u_r) to a good approximation. The velocity is measured in the platform reference frame which holds the cameras, but for a better connection with modelling, we convert them to the initial reference frame by subtracting the velocity increment $v_0 = r_0\Delta\Omega$ to the azimuthal component.

2.2.3. *Temperature measurements*

Temperature profiles are obtained using three vertically profiling thermistor probes mounted on a motor-driven gantry positioned along a tank radius. The probes are equally spaced at 1 m intervals, sampling at radial distances of 1.5 m, 2.5 m, and 4 m from the outer boundary. They are deliberately placed at the opposite azimuthal position with respect to the S-PIV measurement plane to minimise disturbance to the velocity field. Each probe traverses the water column at 5 $\text{cm}\,\text{s}^{-1}$ with an acquisition frequency of 140 Hz. The raw profiles are interpolated onto a regular temporal–vertical grid with resolutions $\Delta t_{\text{Temp}} = 0.01$ s and $\Delta z_{\text{Temp}} = 1$ mm.

Figure 3 shows representative temperature profiles at several times during EXP-S (no rotation) and EXP-SR (with rotation). In both cases, the initial profile (dashed) exhibits a nearly linear temperature gradient over the lower 25–30 cm, capped by a well-mixed upper layer resulting from convection at the water–air interface. As the experiment progresses, the bottom stress erodes the stratification from below: the temperature profiles develop a growing

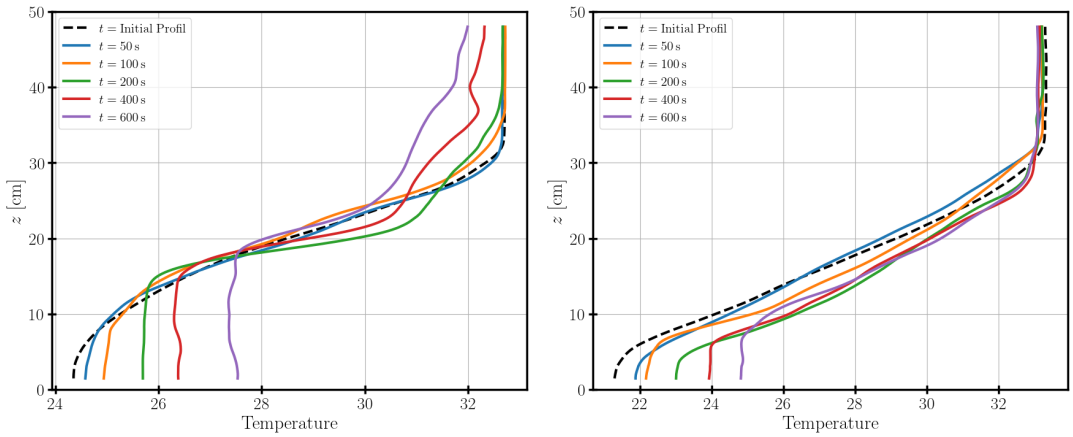

Figure 3. Vertical profiles of temperature for different time during the acquisition. Each color mark a different time of the experiment. The dark dashed line shows the initial profile of stratification prior to the experiment. For both figure, the temperature probe is at 4 m (resp. 2.5 m) from the center (resp. the lateral boundary) of the tank. Left: Experiment without initial rotation (EXP-S). Right: Experiment with initial rotation (EXP-SR).

isothermal layer near the floor, whose upper boundary marks the base of the mixed layer. The deepening is markedly faster in the non-rotating case (EXP-S), where the mixed layer reaches approximately 20 cm after 600 s, than in the rotating case (EXP-SR), where the Coriolis force limits the vertical penetration of momentum and the mixed layer remains significantly shallower over the same duration. This contrast between the two experiments illustrates the controlling role of rotation on mixed-layer deepening and motivates the quantitative analysis presented in Section 4.

2.3. *Non-dimensional parameters*

We consider the flow produced in a cylindrical tank of radius $R = 6.5$ m and depth $H = 0.5$ m by a sudden change of rotation rate from Ω_i to $\Omega_f = \Omega_i + \Delta\Omega$. The large aspect ratio $R/H = 13$ ensures that the dynamics are controlled by local vertical fluxes, with negligible influence of the lateral boundary, at least during the initial phases of the spin-up. It is natural to express all horizontal length scales in terms of the measurement radius $r_0 = 4.5$ m $= 0.69\,R$. The aspect ratio is then defined as

$$a = \frac{r_0}{H} = 9 \tag{3}$$

In the initial state of solid-body rotation, the free surface is in equilibrium with the centrifugal force and takes the shape of a paraboloid, with elevation $z = H + \Omega_i^2 r^2/(2g)$. For the present value $\Omega_i = 0.05$ rad s^{-1}, the elevation difference between the center and the outer edge at $r = 6.5$ m is at most $\sim$5 mm, so the free surface can be treated as effectively flat.

The relevant physical parameters are the rotation rate increment $\Delta\Omega$, the Coriolis parameter $f = 2\Omega_i$, the kinematic viscosity of water, the depth H, the radius r_0, and the time t, the buoyancy frequency N, and the diffusivity of heat κ. We discuss here the relevant non-dimensional parameters that we can form with these quantities.

We define the Rossby number Ro based on the rotation rate increment

$$Ro = \frac{\Delta\Omega}{\Omega_i}\,. \tag{4}$$

In our experiments, $Ro \approx 1$, which indicates that the impulsive forcing is of the same order as the background rotation. We define the Reynolds number Re_δ based on the wall velocity

$v_0 = r_0\Delta\Omega$ and the laminar Ekman layer thickness $\sqrt{\nu/\Omega_i}$:

$$Re_\delta = \frac{r_0\Delta\Omega}{\sqrt{\nu\Omega_i}}\,. \tag{5}$$

The Reynolds number based on the laminar Ekman layer thickness is $Re_\delta \approx 10^3$ (computed with $\nu = 10^{-6}$ m^2 s^{-1}), well above the threshold for the transition to turbulence in Ekman layers ($Re_\delta \gtrsim 150$, Lingwood 1996, Sous et al. 2013), confirming that the boundary layer is fully turbulent throughout the experiments. The same value $Re_\delta = 1000$ was used in the DNS of Marlatt et al. (2012), which provides evidence of a fully developed turbulent regime.

A more intrinsic Reynolds number can be formed from the friction velocity u_* and the turbulent Ekman layer thickness $\propto u_*/f$:

$$Re_* = \frac{u_*^2}{f\nu}. \tag{6}$$

This quantity (also called 'friction Rossby number') is not directly controlled by the experimental parameters but is estimated a posteriori from the velocity measurements (by Eq. (1)). The friction Reynolds number, estimated a posteriori is $Re_* \approx 10^3$, comparable to values reported in DNS studies of the turbulent Ekman layer (Marlatt et al. 2012, Braun et al. 2020).

The Ekman number $E_k = \nu/(fH^2)$ also characterises the effect of viscosity in rotating flows. In the laminar regime it sets the Ekman layer thickness as $\delta/H = E_k^{1/2}$ and the Ekman spin-up time as $\Omega_i\tau_E = E_k^{-1/2}$. Its relevance in the turbulent regime is less clear. For our experiment, we have $Ek \approx \mathcal{O}(10^{-5})$. The Ekman number is related to our parameters by $E_k = Ro^2 Re_\delta^{-2} a^{-2}$.

The time t is naturally expressed in units of the inertial period: $\Omega_i t$ when $\Omega_i \neq 0$, or $\Delta\Omega\, t$ otherwise. Three successive phases of the motion can be distinguished:

(i) $\Delta\Omega\, t < \pi$: the influence of fluid trajectory curvature is small and the flow can be treated as rectilinear.

(ii) $\Omega_i t \sim 2\pi$ (or $\Delta\Omega\, t \sim 2\pi$ if $\Omega_i = 0$): an Ekman layer (or von Kármán layer) is established after the damping of a few inertial oscillations, while the bulk flow remains largely unchanged.

(iii) $\Omega_i t \gg 2\pi$ (or $\Delta\Omega\, t \gg 2\pi$ if $\Omega_i = 0$): the bulk flow progressively spins up under the effect of bottom friction.

The values of the non-dimensional numbers can be compared to typical oceanic conditions. In the ocean bottom boundary layer over continental shelves, the friction velocity is of order $u_* \sim 0.5$–2 cm s^{-1} (Perlin et al. 2005) and the Coriolis parameter is $f \sim 10^{-4}$ s^{-1}. The turbulent Ekman depth $\delta_E \sim u_*/f$ is thus of order 10–100 m in the ocean, compared to $\sim$ 5–10 cm in our experiments. With the kinematic viscosity $\nu \sim 10^{-6}$ m^2 s^{-1} this yields $Re_* = u_*^2/(f\nu) \sim 10^7$–$10^8$ in the ocean, several orders of magnitude larger than in the laboratory. However, the transport properties are expected to become independent of the Reynolds number as long as the flow is fully turbulent. Similarly, the Ekman number is several orders of magnitude larger in the laboratory than in the ocean ($E_k \sim 10^{-8}$), both regimes are expected to lie within the fully turbulent asymptote, where transport properties become independent of E_k.

The influence of stable density stratification is quantified by the Richardson number based on the velocity $r_0\Delta\Omega$ and the fluid depth H:

$$Ri = \frac{N^2}{a^2\Delta\Omega^2}. \tag{7}$$

The Richardson number ranges from 0 (EXP-REF) to ≈ 0.4 (EXP-SR), placing the stratified

experiments in the weakly stratified limit where rotation rather than buoyancy controls the boundary layer depth. We can also define a Richardson number Ri_* based on the thickness u_*/f instead of H,

$$Ri_* = \left(\frac{N u_*}{f v_0}\right)^2 . \tag{8}$$

In our experiments $N/f \sim 3$ while $u_*/v_0 \sim 1/20$, so that $Ri_* \sim 0.02$. Therefore, stratification has little influence in the dynamics of the Ekman layer. We will use the temperature as a quasi-passive scalar field.

The Prandtl number, ratio of kinematic viscosity to thermal diffusivity, is $Pr \simeq 6$ for water, in contrast with $Pr \simeq 700$ for salinity. Since the present study focuses on momentum dynamics and the stratification remains weak ($Ri \lesssim 0.4$), the precise value of Pr has presumably a negligible influence on the results.

Alternative choices of non-dimensional parameters are possible. In particular, the final rotation rate Ω_f could be used instead of Ω_i. The general problem of a steady boundary layer between a fluid rotating at Ω_i and a plate rotating at Ω_f has been analysed by Lingwood (1996), providing both the steady solutions and their instability properties. This general case, called BEK, encompasses as special cases the von Kármán layer ($\Omega_i = 0$), the Bödewald layer ($\Omega_f = 0$), and the Ekman layer recovered in the limit $\Omega_f \to \Omega_i$. Their analysis suggests using a weighted average of Ω_i and Ω_f, which reduces to $0.5(\Omega_i + \Omega_f)$ near the Ekman limit. However, the initial stage of spin-up studied here is more strongly influenced by Ω_i, which justifies our choice in Eqs. (4)–(5). This is further supported by Sous et al. (2013), who found experimentally that wall friction depends primarily on Ω_i in the turbulent regime.

3. Theory of the transient Ekman layer in the rotating tank configuration

3.1. *Extended 1D model for axisymmetric cases*

We can describe our experiments in terms of a one dimensional model along the vertical, starting from the Boussinesq equations for an axisymmetric flow in a rotating reference frame with Coriolis parameter f. In cylindrical coordinates, the incompressibility condition writes

$$\frac{1}{r}\frac{\partial (r u_r)}{\partial r} + \frac{\partial u_z}{\partial z} = 0 \, , \tag{9}$$

and the dynamical equations for the velocity components (u_r, u_θ, u_z) and the buoyancy $b = -g(\rho - \rho_0)/\rho_0$ write

$$\frac{\partial u_r}{\partial t} + u_r \frac{\partial u_r}{\partial r} + u_z \frac{\partial u_r}{\partial z} - \frac{u_\theta^2}{r} - f u_\theta + \frac{1}{\rho_0}\frac{\partial p}{\partial r} = \frac{\partial}{\partial z}\left(\nu_t \frac{\partial u_r}{\partial z}\right) \tag{10a}$$

$$\frac{\partial u_\theta}{\partial t} + u_r \frac{\partial u_\theta}{\partial r} + u_z \frac{\partial u_\theta}{\partial z} + \left(f + \frac{u_\theta}{r}\right) u_r = \frac{\partial}{\partial z}\left(\nu_t \frac{\partial u_\theta}{\partial z}\right) \tag{10b}$$

$$\frac{\partial u_z}{\partial t} + u_r \frac{\partial u_z}{\partial r} + u_z \frac{\partial u_z}{\partial z} + \frac{1}{\rho_0}\frac{\partial p}{\partial z} - b = \frac{\partial}{\partial z}\left(\nu_t \frac{\partial u_z}{\partial z}\right) \tag{10c}$$

$$\frac{\partial b}{\partial t} + u_r \frac{\partial b}{\partial r} + u_z \frac{\partial b}{\partial z} = \frac{\partial}{\partial z}\left(\kappa_t \frac{\partial b}{\partial z}\right) . \tag{10d}$$

We have introduced an eddy viscosity ν_t, and diffusivity κ_t for the vertical turbulent transport, but neglected the corresponding horizontal turbulent flux because of the large aspect ratio

condition $a \gg 1$. Note that in the rotating frame, the centrifugal force $\rho\Omega^2/r$ is exactly balanced by an additional radial pressure gradient; these two terms cancel and are therefore omitted in Eq. (10a).

Initially, the fluid and bottom plate ($z = 0$) are at rest (or in solid-body rotation). Taking this state as the reference frame, the velocity is zero everywhere for $t < 0$. At $t = 0$, the bottom plate is impulsively set to rotate at an angular velocity $\Delta\Omega$, while the velocity remains zero far from the boundary layer ($z \to \infty$). Since the geometry is axisymmetric, it is natural to seek solutions with u_r, u_θ proportional to r. Introducing a reference radius r_0, we write

$$u_r = \frac{r}{r_0}\, u(z,t) \;\;,\;\; u(0,t) = 0 \tag{11a}$$

$$u_\theta = \frac{r}{r_0}\, v(z,t) \;\;,\;\; v(0,t) = r_0\, \Delta\Omega \;\; \text{for } t > 0 \tag{11b}$$

$$u_z = w(z,t) \;\;,\;\; w(0,t) = 0 \tag{11c}$$

$$b = b(z,t) \;\;,\;\; \frac{\partial b}{\partial z}(0,t) = 0 \tag{11d}$$

Then Eq. (9) and (10) become

$$2\frac{u}{r_0} + \frac{\partial w}{\partial z} = 0 \tag{12a}$$

$$\frac{\partial u}{\partial t} + w\frac{\partial u}{\partial z} + \frac{u^2 - v^2}{r_0} - fv + \frac{r_0}{r}\frac{1}{\rho_0}\frac{\partial p}{\partial r} = \frac{\partial}{\partial z}\left(\nu_t \frac{\partial u}{\partial z}\right) \tag{12b}$$

$$\frac{\partial v}{\partial t} + w\frac{\partial v}{\partial z} + \left(f + \frac{2v}{r_0}\right) u = \frac{\partial}{\partial z}\left(\nu_t \frac{\partial v}{\partial z}\right) \tag{12c}$$

$$\frac{p}{\rho_0} = \frac{p_\infty(r)}{\rho_0} + \int_z^\infty \left(\frac{\partial w}{\partial t} + w\frac{\partial w}{\partial z} - b\right)\, dz + \frac{w_\infty^2}{2} - \nu_t\, \frac{\partial w}{\partial z}\bigg|_{z=0} \tag{12d}$$

$$\frac{\partial b}{\partial t} + w\frac{\partial b}{\partial z} = \frac{\partial}{\partial z}\left(\kappa_t \frac{\partial b}{\partial z}\right) \tag{12e}$$

For a viscosity ν_t and diffusivity κ_t depending only on z, this is a one-dimensional system of equations in terms of the coordinate z. The pressure is the sum of a term depending only on z (the hydrostatic pressure), and a term $p_\infty(r)$, equal to zero with our hypothesis of vanishing velocity away from the boundary layer. This columnar model represents an Ekman boundary layer in unsteady regime, modified by the radial acceleration and transport effects due to the fluid rotation rate. In this columnar model, the buoyancy has no direct action on the mean velocity. It acts only on the turbulent kinetic energy, which influences the mean flow through the eddy viscosity.

Three phases of motion can be distinguished as stated in section 2.3.

(i) $\Delta\Omega\, t < \pi$: At short times, smaller than the half inertial period π/f, the radial velocity and non-linear terms in Eq. (12c) are negligible. The azimuthal velocity is driven by the bottom friction like in a unidirectional flow. Then the momentum balance can be expressed in terms of the displacement thickness

$$\delta_1 = \frac{1}{v_0}\int_0^\infty v\, dz \tag{13}$$

This thickness increases under the effect of wall stress ρu_*^2 as $d\delta_1/dt = u_*^2/v_0$. For a constant friction coefficient $C_\delta = u_*^2/v_0^2$, this results in the linear growth with time t,

$$\delta_1 = C_\delta \, v_0 \, t \tag{14}$$

(ii) $\Omega_i t \sim 2\pi$ (or $\Delta\Omega \, t \sim 2\pi$ if $\Omega_i = 0$): After a time approaching half an inertial period, a radial velocity u appears, and the momentum balance is modified by the Coriolis term fu. This leads to a steady Ekman layer, or to a more general Bodewald-Ekman-Karman layers if we include the local Coriolis effect associated with the angular velocity $\sim v_0/r_0$. This will be further discussed in section 3.2.

(iii) $\Omega_i t \gg 2\pi$ (or $\Delta\Omega \, t \gg 2\pi$ if $\Omega_i = 0$): At still later times the friction effect at the bottom is progressively transferred to the fluid column by Ekman pumping effects, as it will be discussed in section 3.3.

To close this 1D set of equations, turbulent viscosity and diffusivity will be computed with the k-ε model, implemented in the GOTM single-column framework (Umlauf and Burchard 2005). Full details of the numerical setup are given in Appendix B. Note that we do not solve Eq. (12) in its full form. First we neglect the radial pressure term, which is valid at the early stage, before the buildup of a significant bulk flow by the spin-up process. We also neglect the vertical advection of momentum which turns out to be negligible in our calculations (see appendix D). In consistency, the advection of TKE by the mean vertical velocity is also neglected.

3.2. *Theory of the transient Ekman layer*

To build physical intuition, we solve analytically the onset of the Ekman layer in the laminar limit ($Ro \to 0$, $Re_\delta \to 0$, $\nu = const.$). Two boundary conditions are considered: an imposed stress, whose exact solution has been already published by Ekman (1905), and an imposed velocity, which is the relevant condition for our laboratory tank and whose solution is derived here to complement Ekman's solution. The comparison of the two reveals that the boundary condition controls the damping rate of inertial oscillations. In the aforementioned limit, the system (12) reduces to

$$\frac{\partial u}{\partial t} - fv = \nu \frac{\partial^2 u}{\partial z^2} \, , \tag{15a}$$

$$\frac{\partial v}{\partial t} + fu = \nu \frac{\partial^2 v}{\partial z^2} \, . \tag{15b}$$

These two equations can be combined into a single equation by introducing the complex velocity $q = u + iv$, which satisfies

$$\frac{\partial q}{\partial t} + ifq = \nu \frac{\partial^2 q}{\partial z^2}. \tag{16}$$

Let us introduce the normalized coordinate z/δ_E, where $\delta_E = \sqrt{2\nu/f}$ is the thickness of the steady Ekman layer. Looking for time oscillating solutions in the form $q = \hat{q}(z)\exp(-i\omega t)$, we get spatial oscillations decaying with z of the form

$$\hat{q}(z) \propto \exp\left[- \frac{(1+i)}{(1-\omega/f)^{1/2}} \frac{z}{\delta_E} \right] \tag{17}$$

Note that the fluid is assumed at rest for large z since the flow is analysed in the rotating reference frame before spin-up, so that u, v exponentially decay for $z \to \infty$. In the alternative case of a uniform geostrophic velocity at large z, the same equation (15) would hold for the

velocity defect, obtained by subtracting the geostrophic velocity to the velocity field (see Eq. 35).

The general solution of (16) can be expressed as an integral over frequencies of such elementary solutions. The weight of each frequency can be obtained as the Fourier transform of the step function representing the boundary condition at $z = 0$. After typically half an inertial period, this integral is quickly dominated by the frequency $\omega = 0$, dominant in the boundary condition, and by the inertial frequency $\omega = f$ which is resonant, as the penetration depth $\delta(\omega) = \delta_E(1 - \omega/f)^{-1/2}$ diverges for $\omega \to f$. Then the solution can be approximately expressed as the sum of the classical steady Ekman layer solution $q_{\rm Ekman}(z)$ and an inertial oscillation whose amplitude $q_{\rm IO}(z,t)$ slowly evolves with time,

$$q(z,t) \simeq q_{\rm Ekman}(z) + q_{\rm IO}(z,t)\ \exp(-ift), \tag{18}$$

The quality of this approximation will be checked below by the exact solution (Fig. 4) and compared with the laboratory experiments in Section 5.

The first term in Eq. (18) is the classical steady state Ekman solution given by (17) for $\omega = 0$, $q_{\rm Ekman}(z) \propto \exp(-z/\delta_E)\ \exp(-iz/\delta_E)$. Equation (17) diverges for $\omega = f$ but the inertial oscillation can be specified by introducing the form $q = q_{\rm IO}(z,t)\exp(-ift)$ in Eq. (16). This eliminates the Coriolis term and yields the pure diffusion equation

$$\frac{\partial q_{\rm IO}}{\partial t} = \nu \frac{\partial^2 q_{\rm IO}}{\partial z^2}. \tag{19}$$

It describes circular particle motion (in the anticyclonic direction) driven by the divergence of the diffusive flux. The amplitude of this circular motion diffuses by viscosity like the linear momentum in the absence of Coriolis effect. This contrasts with the steady component whose penetration is inhibited by Coriolis effects. Therefore the inertial oscillation will eventually penetrate deeper than the steady component, forming a slab of circular motion whose thickness spreads as $\delta_{IO} \propto (\nu t)^{1/2}$.

The behaviour then depends on the boundary condition at $z = 0$. We shall distinguish the case of an imposed velocity v_0 and the case of an imposed shear stress u_*^2, for $t > 0$,

$$\begin{aligned} \text{imposed stress}: &\quad \nu\frac{\partial v}{\partial z} = -u_*^2\,, \quad \nu\frac{\partial u}{\partial z} = 0 \\ \text{imposed velocity}: &\quad v = v_0\,, \quad u = 0\,. \end{aligned} \tag{20}$$

The steady component for a given velocity $v = v_0$ is given by

$$q_{\rm Ekman}(z) = iv_0\ \exp\left[-(1+i)\frac{z}{\delta_E}\right]. \tag{21}$$

The corresponding viscous stress $-\nu\partial q_{\rm Ekman}/\partial z$ has the same form but is tilted by an angle $\pi/4$.

$$-\frac{\partial q_{\rm Ekman}}{\partial z} = i\frac{v_0}{\delta_E}\ \sqrt{2}\ \exp\left(i\frac{\pi}{4}\right)\ \exp\left[-(1+i)\frac{z}{\delta_E}\right]. \tag{22}$$

The value of this shear stress at the boundary is $u_*^2 = \nu v_0/(\delta_E\sqrt{2})$, tilted by $\pi/4$ with respect to the y axis. Therefore, Eq. (21) is also the solution of the problem with this imposed shear stress.

However, the inertial oscillation behaves differently in each case. Indeed, by vertical integration of (19), we get

$$\frac{d}{dt}\int_0^\infty q_{\rm IO}dz = -\nu\ \frac{\partial q_{IO}}{\partial z}\bigg|_{z=0}. \tag{23}$$

A boundary condition of given shear stress $-\nu\frac{\partial q}{\partial z}\Big|_{z=0}$ will result in a zero average of the oscillating component $\nu\partial q_{IO}/\partial z = \nu\frac{\partial q}{\partial z}\exp(ift)$. Therefore, the integral $\int_0^\infty q_{\rm IO}dz$ is conserved. Since the thickness of the inertial oscillation increases by diffusion as $\delta_{IO} \propto (\nu t)^{1/2}$, the amplitude of the oscillation also decreases in $\propto (\nu t)^{-1/2}$. There is no such clear argument for the no-slip solution: we need the exact solution to analyse the decay of inertial oscillations.

We turn now to the exact solution of (16) for the stepwise surface forcing. The imposed stress solution has already been published in the seminal article of Ekman (1905) (the mathematical solution is acknowledged as a contribution of I. Fredholm). The approach relies on the Green's function of (16), which describes the response to an impulsive forcing applied at time $t_i < t$ and takes the form

$$q(z,t) = \frac{q_0}{\sqrt{t'}}\exp(-ift')\ \exp\left(-\frac{z^2}{4\nu t'}\right)\,, \tag{24}$$

where $t' = t - t_i$ (this is the elementary solution of the diffusion equation (19) for the variable $q\ \exp(ift)$).

Then the solution for the sudden shear stress set at $t > 0$ is obtained as an integral of this elementary solution over all time origins t_i in the range $[0\ \ t]$. It yields the following integral over the time delay, expressed in terms of the non-dimensional time $\tau' = ft'$,

$$q(z,t) = \frac{iu_*^2}{\sqrt{\pi}(\nu f)^{1/2}}\int_0^{ft}\frac{\exp(-i\tau')}{\tau'^{1/2}}\ \exp\left(-\frac{fz^2}{4\nu\tau'}\right)\ d\tau'\,. \tag{25}$$

The prefactor has been adjusted to fit the shear stress condition at $z = 0$ as justified below. After taking the real and imaginary parts, it corresponds to Eq. (10) of Ekman (1905). This is the exact solution of the transient problem. It can be interpreted as a sum of inertial oscillations with amplitude and phase depending on ζ.

The shear stress $-\nu\partial q/\partial z$ is then expressed as

$$-\nu\frac{\partial q}{\partial z} = \frac{iu_*^2}{\sqrt{2\pi}}\int_0^{ft}\frac{\exp(-i\tau')}{\tau'^{3/2}}\ \frac{z}{\delta_E}\ \exp\left(-\frac{fz^2}{4\nu\tau'}\right)d\tau'\,. \tag{26}$$

This expression should tend to the step function (Heaviside function) in the limit $z \to 0$. This limit is not obvious since the integrand diverges for $\tau' \to 0$. It can be obtained by making the change of variable $X = (z/\delta_E)\tau'^{-1/2}$, such that $d\tau' = -2(z/\delta_E)^2X^{-3}dX$. Then (25) becomes, reversing the bounds of the integral obtained with the new variable,

$$-\nu\frac{\partial q}{\partial z} = iu_*^2\sqrt{\frac{2}{\pi}}\int_{(z/\delta_E)(ft)^{-1/2}}^{\infty}\exp\left(-\frac{X^2}{2} - i\frac{z^2}{\delta_E^2X^2}\right)\ dX\,. \tag{27}$$

The integral now converges for any z, and for $z \to 0$, it tends to $\int_0^\infty \exp(-X^2/2)\ dX = \sqrt{\pi/2}$. Therefore, the imaginary part of $-\nu\partial q/\partial z$ is equal to u_*^2 for $t > 0$, while its real part is equal to 0, which fits with the boundary condition (20) for imposed stress.

The case of imposed velocity can be deduced from Eq. (25) by noticing that if $q(z,t)$ is a solution of (16), then $\partial q/\partial z$ is also a solution, thanks to the commutation of the partial derivatives with respect to time and space. Thus, we switch from the case of imposed stress to the case of imposed velocity by the transform

$$q\ \to\ -\frac{v_0\nu}{u_*^2}\frac{\partial q}{\partial z}\,. \tag{28}$$

Thus we immediately deduce from (27) a solution for an imposed velocity v_0,

$$q(z,t) = \frac{iv_0}{\sqrt{2\pi}}\int_0^{ft}\frac{\exp(-i\tau')}{\tau'^{3/2}}\ \frac{z}{\delta_E}\ \exp\left(-\frac{fz^2}{4\nu\tau'}\right))d\tau'\,. \tag{29}$$

The main difference with the original solution (Eq. 25) derived by Ekman is the exponent of the decay time ($\tau^{-1/2}$ for the free-slip solution and $\tau^{-3/2}$ for the no-slip solution), such that the damping rate is very different in the two cases.

We have numerically determined the solution (25) for an imposed wall stress and the solution (29) for the no-slip case. The reduced coordinate $\zeta = z/\delta_E$ is used. In the latter case, we choose a unit velocity $v_0 = 1$, and in the former case a wall condition $-\partial|q|/\partial\zeta = \sqrt{2}$ tilted by an angle $\pi/4$ so that the final steady state is the same in both cases. As anticipated, we observe a much faster decay of the inertial oscillations in the no-slip case. This is visualized in Fig. 4 by plotting the two velocity components at altitude $\zeta = 1$, for which the two velocity components are equal in the steady regime. Although we have not made any hypothesis about the separation of the steady regime and inertial oscillation, the exact solution appears as a clear superposition of the two solutions.

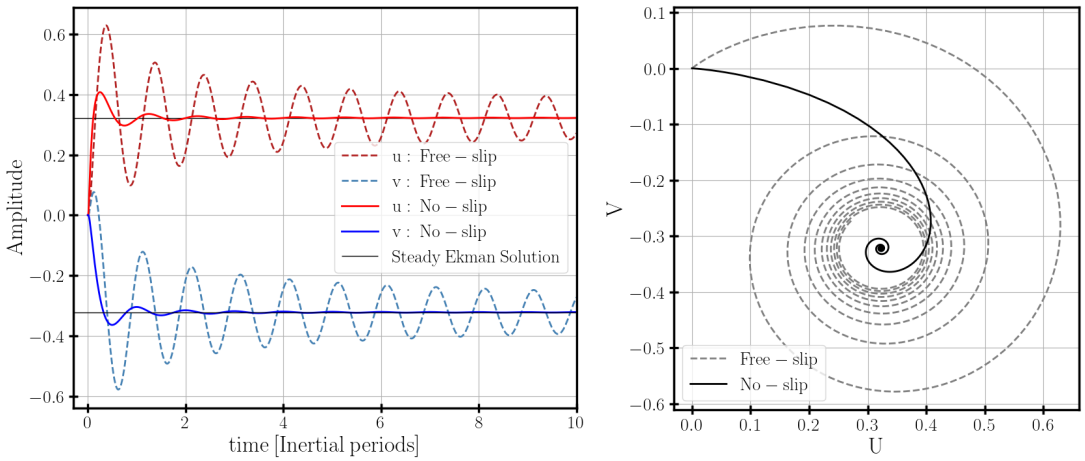

Figure 4. Damping of Inertial Oscillation for linear Oscillatory Ekman Layer. Left: resolution of Eq. (29), in solid line, for a velocity impose at the boundary in the $x-$direction. In dashed line the resolution of Eq. (25) for a shear stress impose (free-stress) at an angle $\pi/4$. For both the solution is computed at $\zeta = 1$. The thin black line display the steady Ekman solution (21). Right: Hodograph for 10 successive inertial oscillations at $\zeta = 1$ for in solid (resp. dashed) line the no-slip (resp. free-slip) condition.

A key question is how these laminar results extend to the turbulent regime. In the limit of large Reynolds numbers, steady flow components are expected to be functions of the reduced vertical coordinate $\zeta = zf/u_*$. This reflects the hypothesis that the properties of turbulence are fully determined by the friction velocity u_* (the eddy viscosity hypothesis is not required). This yields a universal velocity profile, the turbulent counterpart of (21), which must be matched with the log layer near the wall (see for instance Garratt 1992).

Although the time-dependent eddy viscosity $\nu_t(z,t)$ couples the mean flow to the oscillating shear, the steady-state Ekman balance is independent of the transient excitation: provided any damping mechanism is present, the inertial oscillations decay and the flow converges to the same steady solution, regardless of the damping timescale. This will be investigated in Section 5 by decomposing the velocity field into a time-mean component and an oscillating residual, and comparing the k-ε simulations with the experimental results. We will show that, despite the slow attenuation of the oscillations, the two contributions remain statistically independent and the time-mean profile converges to the turbulent Ekman spiral.

In a turbulent boundary layer, the eddy viscosity ν_t vanishes as $\nu_t \sim \kappa u_* z$ in the log layer and drops to zero at $z = 0$, where the flow is locally laminar within the viscous sublayer. As a consequence, the effective stress transmitted to the fluid is neither the large no-slip viscous stress (which would require resolving the sublayer) nor zero (as in free-slip), but an

intermediate value set by the quadratic drag law

$$\tau_b = C_f |\mathbf{u}_1| \mathbf{u}_1 \,, \tag{30}$$

where $\mathbf{u}_1$ is the velocity within the log layer. This drag law encodes the integrated effect of the unresolved viscous sublayer through the empirical coefficient C_f.

The damping rate of the inertial oscillations is therefore controlled by C_f: a larger drag coefficient extracts momentum more efficiently from the oscillating flow and accelerates the decay, while a smaller one allows the oscillations to persist longer. In the no-slip laminar limit, the effective $C_f \to \infty$ (the velocity is pinned to zero at the wall), leading to rapid damping. In the free-slip limit, $C_f = 0$ and there is no damping from the boundary. The turbulent regime, with a finite C_f, naturally interpolates between these extremes.

It is worth noting that this mechanism is not specific to the laboratory setting: in the oceanic boundary layers, the same quadratic drag law governs the dissipation of near-inertial energy, and the value of C_f directly controls the persistence of inertial oscillations generated by impulsive wind or tidal forcing.

The goal of our laboratory experiments is to extend the laminar picture to the turbulent regime, where the bottom boundary condition is no longer a strict no-slip but is governed by the quadratic drag law, as discussed in Section 5.

3.3. *Ekman pumping effects*

In the absence of buoyancy effects, the resulting azimuthal velocity away from the wall $v_\infty(r,t)$ can be assumed independent of z. This results from the shallow water geometry, with height H smaller than the radius r, and the Taylor column effect due to rotation. Then the time evolution of the bulk azimuthal velocity v_∞ can be obtained by vertical integration of Eq. (10b). In a first approximation the water column momentum $\int_0^H u_\theta dz \simeq H v_\infty$ is locally driven by wall friction

$$H \frac{\partial v_\infty}{\partial t} = -\nu_t \frac{\partial u_\theta}{\partial z}_{(z=0)} = u_*^2 \,. \tag{31}$$

To refine this expression, we need to take into account additional terms due to advection by vertical and radial velocities. Assuming a fixed upper surface, the integral of u_r then vanishes by mass conservation. Furthermore, using (9), we can express $u_z \partial u_\theta/\partial z = \partial(u_\theta u_z)/\partial z + (u_\theta/r)\partial(r u_r)/\partial r$. The vertical integral of the first term vanishes by the boundary conditions $u_z = 0$ at $z = 0$ and $z = H$, while the second term adds to $u_r \partial u_\theta/\partial r$. Then, the vertical integral of Eq. (10b) can be expressed as

$$H \frac{\partial v_\infty}{\partial t} = u_*^2 - \frac{1}{r^2} \frac{\partial}{\partial r} \int r^2 u_r u_\theta \, dz \tag{32}$$

The second term represents the divergence of the radial advection of angular momentum. With the scaling (11), the latter is equal to $(4/r_0) \int uv dz$. Since $\int u dz = 0$, this can be also written as $(4/r_0) \int u(v - v_\infty) dz$. For spin-up, the radial velocity within the boundary layer is outward ($u > 0$), while $v - v_\infty > 0$, so that it is opposed to the driving force[1]. This radial transport term is quadratic in velocity like the wall friction u_*^2. Therefore, the right hand term of (32) can be empirically modeled as

$$H \frac{dv_\infty}{dt} = C_b (v_0 - v_\infty)^2 \,, \tag{33}$$

[1]For spin-down, $u < 0$, while $v - v_\infty < 0$, so it enhances the driving force (negative in this case).

where v_0 is the wall velocity. This integrates in time as

$$v_\infty = v_0 \frac{(C_b v_0/H)\, t}{1 + (C_b v_0/H)\, t}, \tag{34}$$

This introduces a characteristic turbulent spin-up time $\tau_{\mathrm{turb}} = H/(C_b v_0)$, which must be compared to the inertial time Ω_i^{-1} to assess the relative importance of rotation and friction in the long-time evolution. The coefficient C_b will be determined experimentally.

4. Mean flow and turbulent statistics

We now examine the mean flow structure and turbulence statistics from the observations, and assess how well they are captured by the proposed scaling framework.

4.1. *Coherent structures*

Figure 5 shows dye visualisations of the boundary layer with and without background rotation, offering a qualitative picture of how rotation reorganises the turbulent boundary layer. In the absence of rotation (Fig. 5, top), large vigorous structures erupt from the bottom and penetrate deep into the interior, reaching heights of 10–12 cm. The dye interface is highly irregular, with mushroom-shaped tilted plumes and overturning billows across a broad range of scales, consistent with the absence of a rotational constraint. Similar patterns are visible in DNS computations of the temporally developing turbulent boundary layer by Kozul et al. (2016).

In the rotating case (Fig. 5, bottom), turbulent activity is confined to a layer of 6–8 cm, consistent with the rotational scaling $\delta_E \sim u_*/f$. The structures are markedly smaller and more regular, the interface sharper and more horizontal, indicative of the suppression of large vertical excursions by rotation and stratification. Kelvin–Helmholtz billows are visible at the interface. The structures in the rotating case hint at some horizontal organisation, possibly reflecting inertial effects reminiscent of the Ekman roll instability documented in DNS studies (Marlatt et al. 2012).

4.2. *Mean flow profiles*

We now turn to a more quantitative analysis of the boundary layer structure, focusing on three configurations: EXP-REF, EXP-S and EXP-SR (cf. Table 1). Stereoscopic PIV measurements provide the three velocity components in a vertical plane aligned with the azimuthal direction. The velocity field has been decomposed into a mean component and a fluctuating component, taking average in the azimuthal direction and a sliding time window (see Appendix A for details). The resulting mean and variance can be interpreted as 1D profiles that allow the comparison with the 1D numerical simulation. We plot the vertical profiles at $t = 100$ s. It is worth stating that at $t = 100$ s the interior flow has already been partially spun up (Fig. 12). Since the interior velocity evolves in time due to the spin-up process, we define a defect velocity as the local velocity from which the interior velocity (measured sufficiently far from the bottom boundary) has been subtracted. Because the interior velocity is not directly accessible from the experimental measurements, we use, as a proxy, the azimuthal velocity averaged over the uppermost centimetre of the measured profile, denoted u_θ^{top}. This defect velocity is therefore defined as

$$\langle u_\theta \rangle - v_\infty \approx \langle u_\theta \rangle - u_\theta^{top}. \tag{35}$$

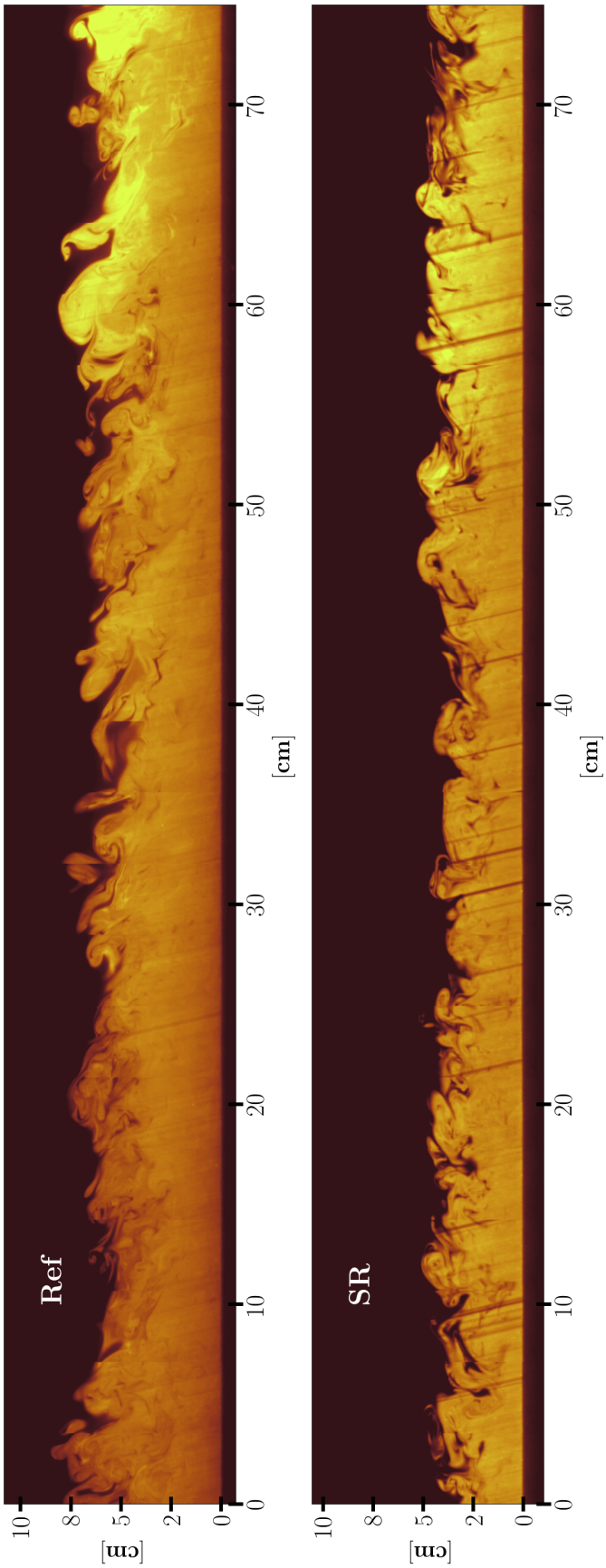

Figure 5. Panoramic reconstruction of the dye-visualised boundary layer over a horizontal extent of 0.75 m, obtained by compositing successive frames spanning $\Delta t = 5$ s. The first frame of each composite is taken at $t = 52$ s after the impulsive spin-up. Note that the contrast has been adjusted independently for each panel to enhance the visibility of the structures. Top: non-rotating, unstratified case (EXP-REF). Bottom: rotating, weakly stratified case (EXP-SR). For both picture, the saturation on the right comes from a brighter illumination of the right part of the laser sheet. Inclined black lines are shadows from clusters of particles on the surface.

The interior velocity has therefore been subtracted so that only the velocity anomaly is shown, with the region beyond the Ekman layer set to zero. Although the viscous sublayer is not resolved in the 1D simulation (see Appendix B), the near-wall grid points agree well with the experimental data in both cases.

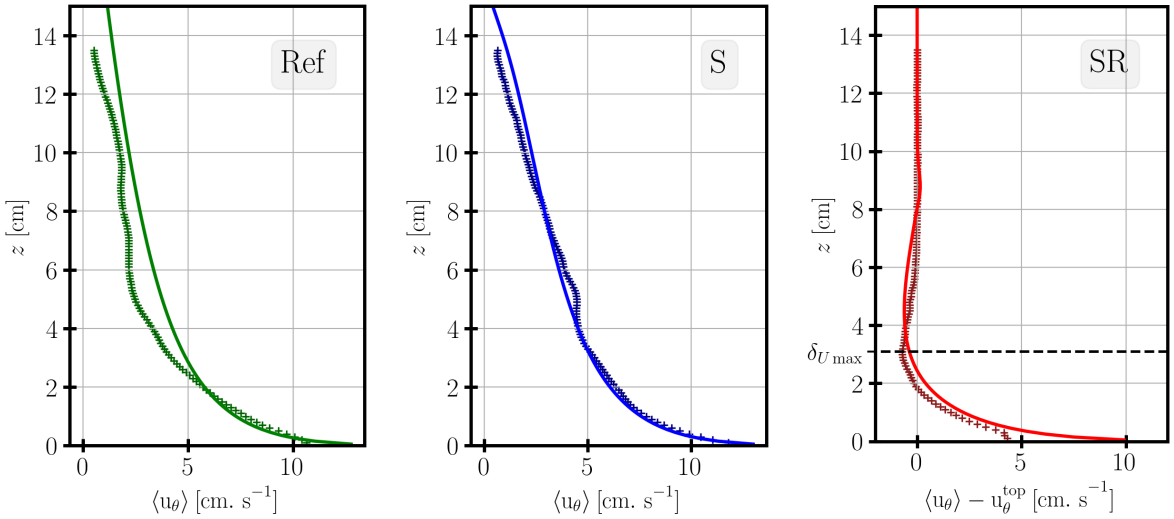

Figure 6. Vertical profiles of azimuthal mean velocity $\langle u_\theta \rangle$ at $t = 100$ s. Experimental data are marked by +. We plot with solid line, the vertical profile from k-ε simulation. Left: Experiment without rotation-without stratification (EXP-REF). Center: Experiment without rotation-with stratification (EXP-S) . Right: Experiment with rotation-with stratification (EXP-SR). For the experiment with rotation, the interior velocity (u_θ^{top}) has been subtracted in order to visualize the velocity anomaly. The horizontal dashed line in the right panel indicates the height of $\delta_{U\,\max}$ where the overshoot is at its maximum value.

We plot in Fig. 6 the azimuthal velocity for the three configurations. In the non-rotating cases, the near-bottom velocity is similar across experiments, reaching $\langle u_\theta \rangle \simeq 7$ cm s^{-1} at $z = 1$ cm. The shear is maximum near the wall, where the no-slip condition imposes $u_\theta = v_0$ at $z = 0$. A rough estimate of the friction velocity follows from $u_*^2 \simeq \nu\, \Delta\langle u_\theta \rangle / \Delta z \simeq 1.6 \times 10^{-4}$ m^2 s^{-2}, consistent with independent estimates from the turbulent momentum flux profile (section 4.4.2). With this estimate, we also recover the scaling $u_*/v_0 \simeq 1/20$ (Sous et al. 2013).

The main differences between the non-rotating and rotating boundary layers appear in the layer above the near-bottom region. Rotation constrains the vertical extent of the boundary layer, with the azimuthal velocity reaching zero near $z = 6$ cm and a super-geostrophic overshoot visible between 2 and 5 cm, whereas the non-rotating boundary layer extends beyond the observation window. The height at which this super-geostrophic velocity reaches its maximum amplitude is defined as $\delta_{U\,\max}$.

This observation is also apparent in the radial velocity profiles (Fig. 7). In the rotating case, the radial velocity is driven primarily by the deflection of the primary geostrophic circulation by the Coriolis force, and the shear is approximately constant throughout the layer, in contrast to the azimuthal component. In the non-rotating case, the agreement between the 1D k-ε model and the experiments is less accurate, which is likely due to the superposition of several dynamical processes contributing to the radial flow at this stage of the spin-up. In particular, the centrifugal acceleration associated with the azimuthal flow drives an outward radial buoyancy flux that depends on the horizontal density gradient between neighbouring columns, which is unavailable to a single-column model. Additionally, the absence of rotation means that there is no Coriolis restoring force to organize the radial flow, leaving it more sensitive to transient effects such as the initial filling of the tank and large-scale recirculation. As discussed in section 3, the centrifugal acceleration cannot be neglected in this configuration. Despite these limitations, the 1D model captures the amplitude and general shape of the

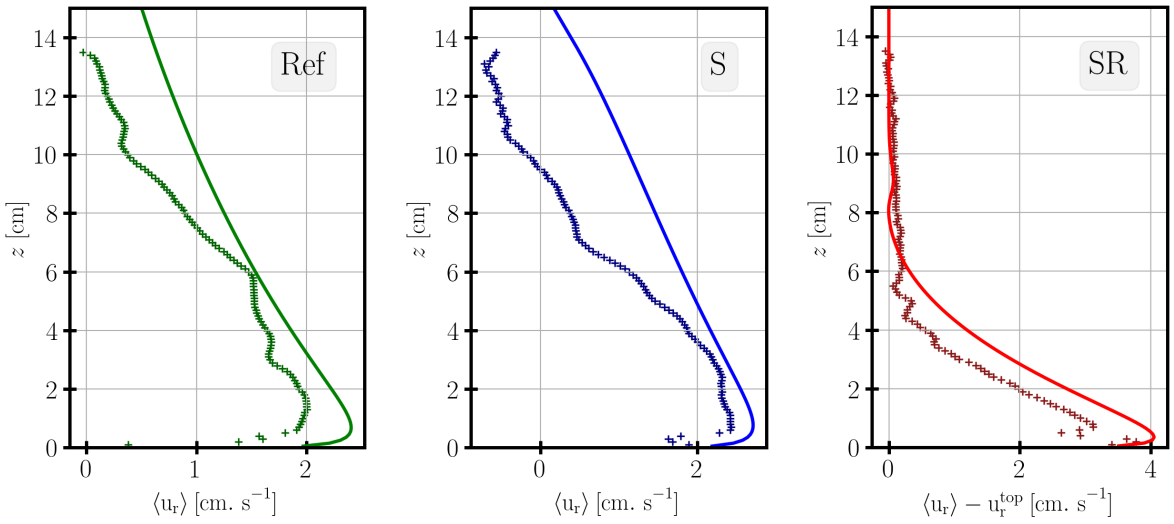

Figure 7. Same as figure 6 but for the radial velocity at $t = 100$ s

vertical profile reasonably well. The similarity between the profiles in EXP-REF and EXP-S confirm that the chosen stratification does not exert a strong control on the dynamics.

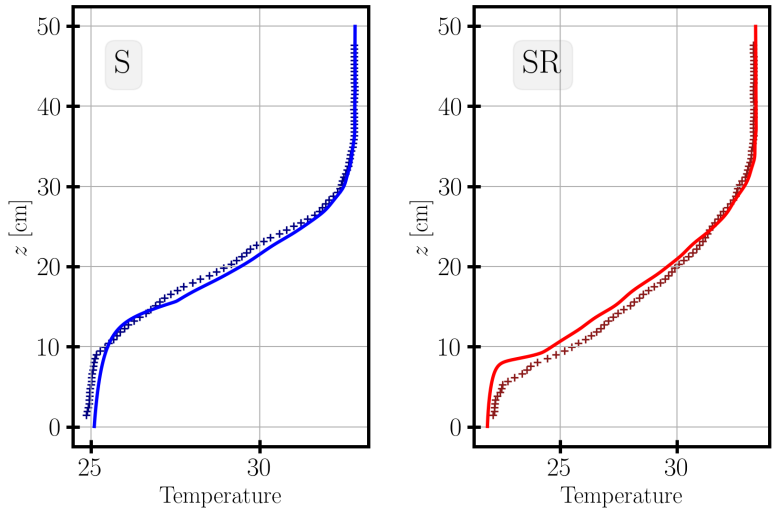

Figure 8. Same as figure 6 but for the temperature profile at $t = 100$ s. The vertical axis is greater than the one for the velocity data.

The vertical confinement by rotation is confirmed by the temperature profiles (Fig. 8). The mixed layer reaches only 6 cm in the rotating case against 13 cm in the non-rotating case despite similar initial stratification. The k-ε model also produces a sharper thermocline interface than observed in the experiments, an effect that is particularly pronounced in the rotating case.

Figure 9 shows the hodograph of the horizontal velocity at $t = 100$ s, in which the Ekman spiral is clearly visible over the observed portion of the water column. The hodograph does not extend to the bottom boundary, so the viscous sublayer and the cross-isobaric angle cannot be directly determined from this plot alone; the missing endpoint corresponds to the no-slip condition at the tank bottom, where $u_r = 0$ and $u_\theta = v_0$. The k-ε model reproduces the overall spiral structure fairly accurately; even if we note that the agreement worsens near the viscous layer, which is neither correctly observed experimentally nor explicitly resolved by the 1D model and which depends, to a certain extent, on a drag coefficient that remains empirical.

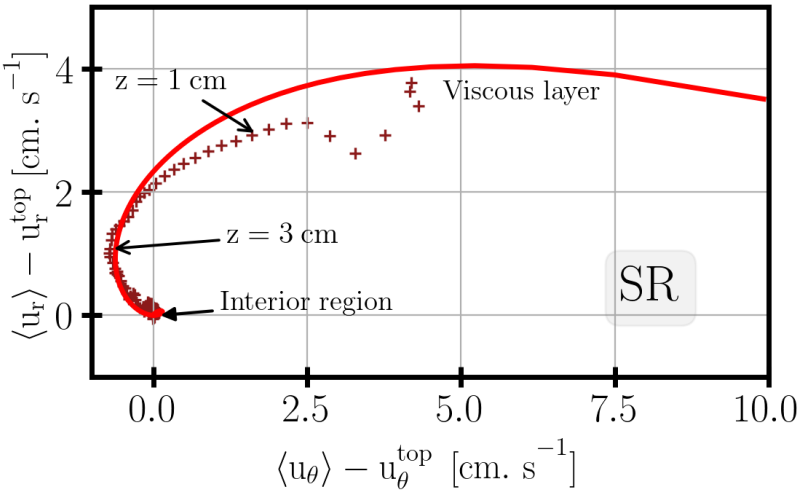

Figure 9. Hodograph of the defect velocity at $t = 100$ s showing the Ekman Spiral (radial vs azimuthal velocity components). Different height (in cm) are indicated by black arrow as the two characteristic region – the Interior region and the Viscous layer. In solid line, the vertical profile from k-ε simulation.Experimental data (SR) are plotted with crosses (+).

4.3. *Calibration of the drag coefficient from the cross-isobaric angle*

The k-ε model requires a value of the drag coefficient C_f appearing in the bottom boundary condition

$$u_*^2 = C_f |\mathbf{u}(z_1) - \mathbf{u_{wall}}|^2 . \tag{36}$$

Although C_f can in principle be estimated from the Law of the Wall as $C_f = [\kappa / \ln(z_1/z_0)]^2$ (see Appendix B), its value depends logarithmically on the ratio z_1/z_0, which is not precisely known a priori because the roughness length z_0 is sensitive to the surface imperfections of the tank floor and to the Reynolds number. It is therefore preferable to calibrate C_f against an independent physical observable.

A natural calibration target is the cross-isobaric angle α_0, defined as the angle between the bottom wall stress $\boldsymbol{\tau}_b$ with respect to the azimuthal wall velocity (this would correspond to the angle of the wall stress to the geostrophic bulk velocity in a reference frame attached to the floor). In the turbulent Ekman layer, this angle is set by the vertical structure of the boundary layer and provides a sensitive integral measure of the eddy-viscosity distribution near the wall.

The DNS study of Marlatt et al. (2012), performed in Cartesian geometry at $Re_* = 1000$, reports a steady-state cross-isobaric angle $\alpha_0^{\mathrm{DNS}} = 18.6°$. This value constitutes a well-established reference against which the k-ε model can be calibrated. To obtain such a cross-isobaric flow, we find $C_f = 5 \times 10^{-3}$ (see Appendix C). This value of C_f is used in all k-ε simulations presented in this paper.

4.4. *Turbulent quantities*

4.4.1. *Turbulent Kinetic Energy (TKE)*

Figure 10 shows the vertical profiles of TKE at $t = 100$ s for the three configurations. In all cases, the TKE decreases monotonically with height, with maximum values near the bottom boundary of order 2–4 cm^2 s^{-2}, reflecting the dominance of bottom-generated shear turbulence. The k-ε model reproduces this near-bottom peak and the overall decay with height, though it predicts a sharper vertical gradient than observed experimentally. The experimental profiles exhibit a more gradual decay, with non-negligible TKE persisting throughout the

mixed layer, likely due to the presence of large-scale turbulent structures not captured by the 1D closure.

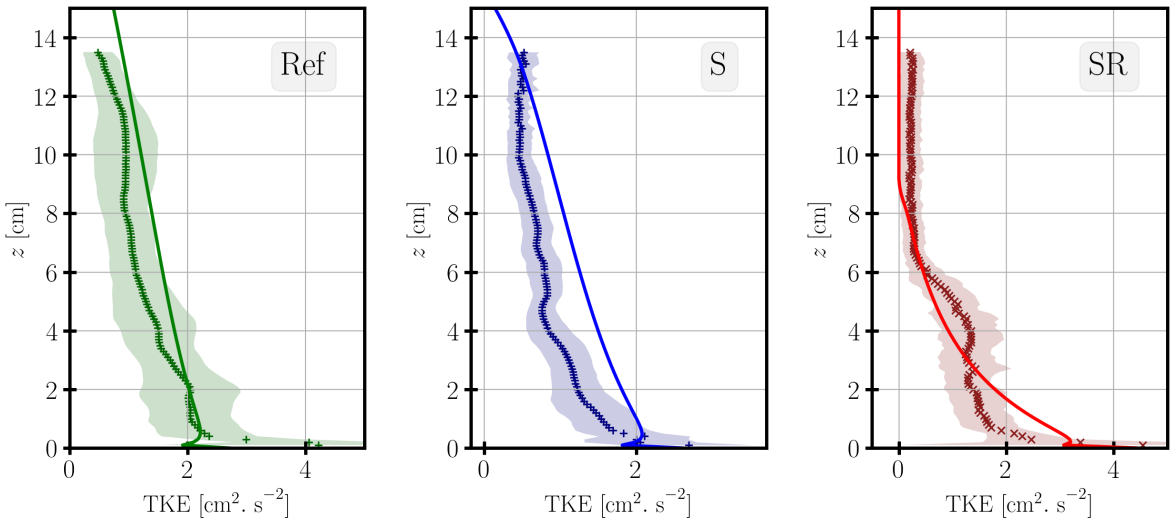

Figure 10. Vertical profiles of TKE at $t = 100$ s. Experimental data, marked by $\times$ are averaged, for each height, over a 10 s,temporal window. The shaded interval represent the variance regarding this averaging. In solid line, the vertical profile from k-ε simulation. Left: Experiment without rotation-without stratification (case REF). Center: Experiment without rotation-with stratification (case S). Right: Experiment with rotation-with stratification (case SR).

In the non-rotating unstratified case (EXP-REF, left panel), the TKE remains significant up to the top of the observation window, consistent with the absence of any mechanism limiting the vertical extent of turbulence. In the rotating stratified case (EXP-SR, right panel), the TKE drops more sharply above $z \approx 6$ cm, consistent with the rotational confinement of the boundary layer observed in the velocity profiles. The k-ε model captures this confinement with a slight overestimate but represents well the near-bottom TKE relative to the measurements.

Note that the shaded area indicates the associated standard deviation of the sliding mean over a 5 s interval. This deviation is calculated at each altitude and, as the observed field moves faster than the turbulence decorrelation time, this measurement is not the deviation of the turbulent fluctuation itself, but rather the estimate of the variance of the statistics. Our sliding time average lacks precision since the mean flow varies on similar time scale as the turbulent fluctuations. To improve the statistics, average on a wider azimuthal range would be needed, or an ensemble average on several experiments. Since EXP-REF and EXP-S are very similar, they provide a crude estimate of this ensemble average.

4.4.2. *Vertical Reynolds stress*

Figure 11 shows the vertical profiles of the azimuthal turbulent momentum flux $\langle u'_\theta u'_z \rangle$ for the three configurations at $t = 100$ s.

In the non-rotating cases (left and middle panels), the flux increases from zero at the bottom boundary, reaches a broad maximum of approximately 0.4–0.5 $\mathrm{cm^2\,s^{-2}}$ near the bottom of the observation window, and decays linearly throughout the mixed layer. This quasi-linear profile is consistent with the transient momentum balance $\partial_t \langle u_\theta \rangle \approx \partial_z \langle u'_\theta u'_z \rangle$: in the absence of a mean pressure gradient, the divergence of the turbulent flux drives the local acceleration of the mean flow. We use the extrapolation of this linear profile to get the value of $u_* = 0.7$ $\mathrm{cm\,s^{-1}}$. The k-ε model reproduces both the amplitude and the shape of the profile well in both non-rotating cases, confirming that the eddy-viscosity closure correctly represents the vertical transport of azimuthal momentum in this regime.

In the rotating stratified case (right panel), the turbulent flux is confined below $z \approx 6$ cm, consistent with the rotational suppression of the boundary layer depth observed in the mean

velocity profiles (Fig. 6) and the mixed-layer thickness (Fig. 8). The flux peaks close to the bottom boundary and decays rapidly with height, reflecting the concentration of shear production within the Ekman layer. Above the layer, the flux drops to near zero, indicating that turbulent momentum transport is effectively shut off by the combined effect of rotation and stratification. The k-ε model captures this confinement accurately.

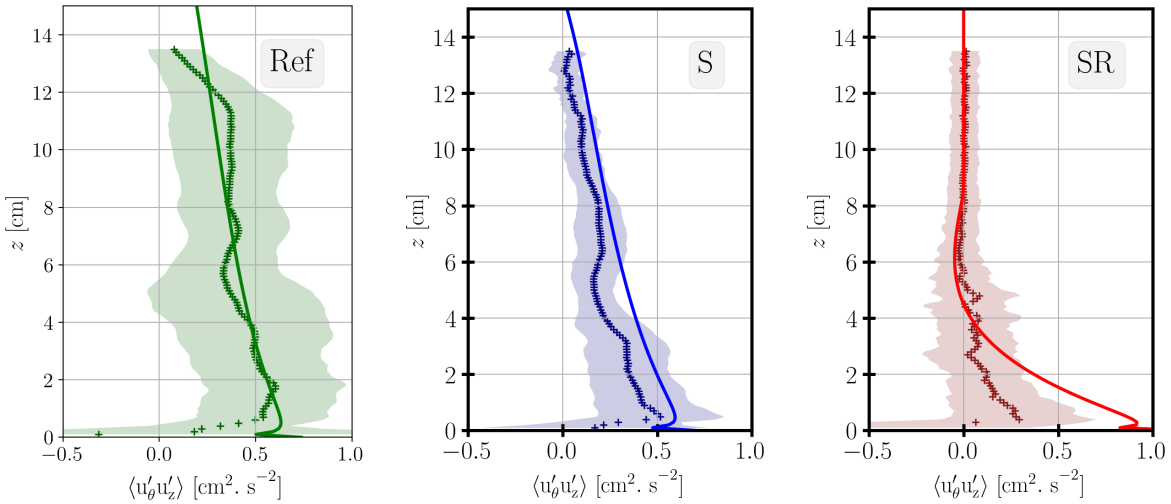

Figure 11. Same as figure 10 but for the vertical turbulent momentum flux $\langle u'_\theta u'_z \rangle$.

The turbulent statistics presented above reflect the same physical picture as the mean profiles: in the non-rotating cases, turbulence fills the entire mixed layer and drives efficient momentum transport, while in the rotating case it is confined within the Ekman layer. This contrast between scalar homogenisation and persistent velocity gradients is physically meaningful: scalars are mixed down-gradient by turbulent diffusion alone, whereas momentum is subject to the additional constraints of rotation and the time-evolving bottom stress. The following section examines how these dynamics evolve in time.

5. Transient evolution of the turbulent Ekman Layer

5.1. *Bulk Spin-up adjustment*

Figure 12 shows a time series of the azimuthal velocity, averaged over the uppermost centimetre of the vertical profile u_θ^{top}. This quantity serves as a proxy for the interior geostrophic velocity noted v_∞ in section 4. In the fluid frame, it increases monotonically toward the platform velocity v_0 as bottom friction spins up the interior flow. The dashed line shows the friction law (Eq. 34), which provides a good fit to the observed decay, yielding $C_b \simeq 2.5 \times 10^{-3}$. Notably, both the rotating (EXP-SR) and non-rotating (EXP-S) cases follow the same friction law, indicating that the spin-up rate and hence C_b are insensitive to background rotation, consistent with the log-layer scaling of the bottom stress. The difference between C_f and C_b is expected: C_f is defined with respect to the near-wall velocity at z_1, which is smaller than the depth-averaged velocity used in the bulk formulation, so that $C_f > C_b$ is consistent with the Law of the Wall. The rotating case shows stronger low-frequency variability, likely due to large-scale structures generated during the filling process in rotation.

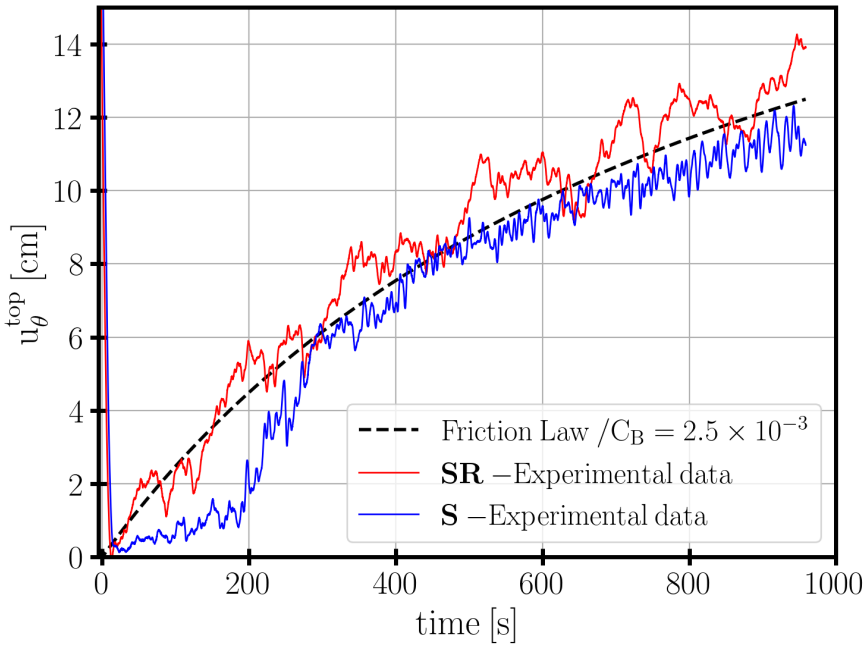

Figure 12. Time series of interior velocity for Spin-up case with (in red) and without (in blue) initial background rotation. The dashed black line correspond to the friction law given in Eq. (34). The interior velocity $\langle u_\theta^{top} \rangle$ is defined by average between 13 and 14 cm above the bottom boundary – the last cm below the upper boundary of the observation window.

5.2. *Evolution of the vertical velocity profile*

Figure 13a shows the temporal evolution of the displacement thickness δ_1 for two non-rotating cases: unstratified (EXP-REF) and weakly stratified (EXP-S). The growth is identical for both cases and follows a linear trend $\delta_1 \propto t$, as expected from momentum conservation in the absence of rotation (see Eq. 14). The fit of experimental data with this linear evolution yields $C_\delta = 10^{-3}$, which corresponds to a ratio $u_*/v_0 \sim 1/30$. This value is smaller than the friction coefficient $C_b \simeq 2.5\ 10^{-3}$ previously obtained for the bulk spin-up over longer times. The value of C_δ is also about twice smaller than the corresponding result of Kozul et al. (2016) from DNS of a temporally evolving turbulent boundary layer. This reflects the fact that both friction and turbulence require some time to become fully established after the impulsive forcing. Based on the experimental curves, this transition phase lasts approximately 20 s. By contrast an initial turbulence level is introduced in the DNS of Kozul et al. (2016), reproducing the effect of a trip wire often used to trigger turbulence in boundary layer studies.

The k-ε model closely follows the experimental measurements. The saturation observed at late times ($t \gtrsim 80$ s) occurs when the boundary layer extends beyond the PIV window, which is the upper limit of the integral. The other reason is also that at this time, the boundary layer begins to feel the effect of rotation and therefore its growth tends to be inhibited, as we will observe in Fig 14.

Note that δ_1 is a low indicator of the boundary layer thickness. An alternative indicator is the height δ_{99} at which the mean velocity reaches 99% of the outer velocity. This characterises roughly the layer with active turbulence. According to the DNS of Kozul et al. (2016), $\delta_1/\delta_{99} = C_1 u_*/v_0$ with $C_1 \simeq 4$, which would yield $\delta_{99} \simeq 6\delta_1$. We cannot reliably measure δ_{99} because of limited measurement precision, but we measure δ_{95} at which the mean velocity reaches 95% of the outer velocity. We find typically $\delta_{95} \simeq 5\delta_1$, in agreement with the experiments with a rotating disk of Imayama et al. (2014), who found $\delta_1 = 0.19\ \delta_{95}$.

We also determine the layer thickness by dye concentration, taking the boundary at the position with maximum gradient of the mean concentration in Fig. 5). This yields a thickness

$\simeq 6\delta_1$, as visible in Fig. 13b. The dye is injected before the experiment through the tank floor as a thin layer of water at temperature 20^oC, in a warmer water above at temperature 22^oC. After some initial mixing it results in a $\sim$ 5 cm thick layer of fluorescent fluid. The corresponding density stratification is wiped out by turbulence once the spin-up is started, so that mixing occurs as a passive scalar. A virtually linear increase from 5 cm to 12.5 cm is observed within 110 s. Beyond this point, once again, the observation is limited by the height of the observation window.

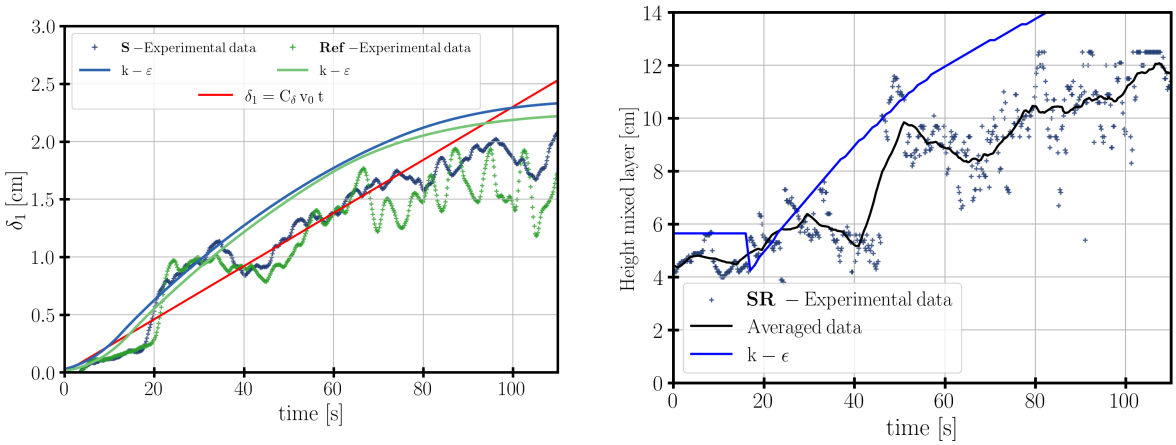

Figure 13. Left: Time evolution of the displacement thickness δ_1 (defined in Eq. 13). Two non-rotating configuration (case Ref and S) are display with + markers and compared with their associated k-ε simulations (in dashed line). The red solid line show the linear fit for $\delta_1 \propto t$ with $C_\delta = 10^{-3}$, and $v_0 = 23.5$ cm .s^{-1}. Right: Time evolution of the height of the mixed layer revealed by the maximum gradient of dye concentration for the Ref case. The thick black line is the average of the experimental data over a neighbour of 10 s.

5.3. *Rotation constraints on boundary layer depth*

In the rotating case (EXP-SR) the azimuthal velocity profile is not monotonic, with a maximum at height denoted $\delta_{U\,\max}$ (see Fig. 6). This height $\delta_{U\,\max}$ then provides a convenient characterisation of the boundary layer thickness. Figure 14(a) shows the temporal evolution of this thickness.

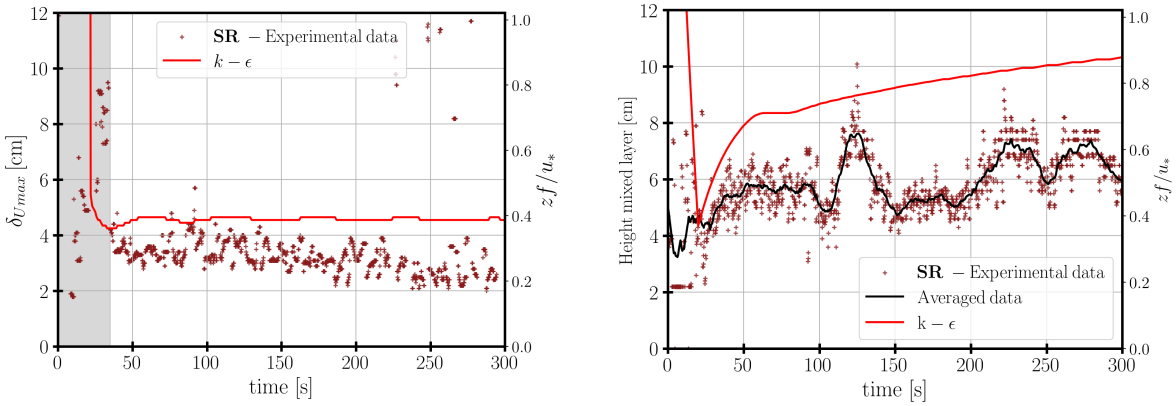

Figure 14. Left: Temporal evolution of the height of the maximum azimuthal velocity $\delta_{U_{max}}$. Right: same as figure 13b for experiment SR with rotation. For both figure, the experimental data marked with + and from the $k - \varepsilon$ model (in solid line) and the adimensional scale on the right y-axis is given for a constant $u_* = v_0/20$ and a constant $f = 0.1$s^{-1}.

Following the step change in rotation rate at $t = 0$, the boundary layer develops from rest and $\delta_{U\,\max}$ grows rapidly. Within the gray shaded area, we observe a linear growth of $\delta_{U\,\max}$

for $0 \lesssim t \lesssim 30$ s: during this early phase, the flow is dominated by turbulent friction and particle trajectories are not yet significantly deflected by the Coriolis force. The large initial values of $\delta_{U\,\max}$ should not be interpreted as a physical overshoot: at early times, before the Ekman veering spiral is established, the velocity maximum is very weak and the diagnostic is ill-defined. At $t \approx 30$ s ($\approx T_f/2$, i.e. half the inertial period) the Coriolis force becomes dynamically significant and the velocity profile develops a clear maximum, marking the onset of the Ekman veering spiral and the transition to a rotationally controlled regime. We see that $\delta_{U\,\max}$ then approaches the known Ekman depth $0.3\,u_*/f$. The result is in reasonable agreement with the k-ε model, which tends to a constant height $\delta_{U\,\max} = 0.4\,u_*/f$. This value is in agreement with the DNS of Marlatt et al. (2012).

At longer times, the experimental data show a gradual thinning of the boundary layer, unlike the model. This thinning is related to the spin-up process, which is not included in the model. Two effects are involved. Firstly, the shear stress u_* decreases as the velocity difference between the floor and the bulk decreases. Secondly, the spin-up increases the effective rotation rate of the fluid, increasing the effective Coriolis parameter f.

Figure 14b shows the corresponding growth of the boundary layer thickness characterised by the dye concentration. This is the counterpart of Figure 13b for a case with rotation. The horizontally inhomogeneous dye injection process does not allow us to observe the very initial growth phase unaffected by rotation. Oscillations observed at later times are attributed to the crossing of large horizontal eddies possibly produced by detachment of the lateral boundary layers. Nevertheless, this figure enables us to demonstrate that the growth of the mixed layer is indeed limited by rotation (and not stratification). It initially stabilises to a value $h \simeq 0.5u_*/f$. The results from the k-ε model is somewhat larger, and a slow thickening persists on longer times. This is due to the diffusion of turbulence away from its shear driven production zone.

We do not observe the further decrease of the thickness observed for $\delta_{U\,\max}$. Indeed the layer of scalar concentration cannot 'un-mix'. Nevertheless, after 300 s, the height reached does not exceed 8 cm.

5.4. *Inertial oscillation in a turbulent regime*

Due to large-scale turbulence, as well as additional motions not directly related to the Ekman adjustment (instabilities, radial transport, Poincaré waves), it is not feasible to perform a reliable strict quasi-stationary/oscillatory decomposition. However, we are able to characterize the inertial response of the Ekman layer using (i) time series at a fixed depth and (ii) depth-integrated transports, which are less sensitive to small-scale intermittency.

5.4.1. *Temporal signature at a given depth*

Figure 15 shows the evolution of the velocity defect ($\langle u_\theta \rangle - u_\theta^{\mathrm{top}}$) at a given altitude ($z = 3$ cm). We observe the onset of an oscillation at the inertial frequency f. Because the observation is not at $z = 0$, the oscillation does not starts at $t = 0$, but start around $t \simeq 10$ s, suggesting that the active layer where the inertial response develops only reaches the observed altitude after a finite time. The shadow zone shows the initial state of the flow previous to the spin-up, we observe the azimuthal velocity is not zero meaning that residual velocities from the fill-up phase are present at the initial state. The progressive decrease of the velocity during this interval coincide with the duration of the incremental angular acceleration. These elements indicate that the structure is passing through the PIV observation window. Since the incremental acceleration is the same as the initial rotation rate ($\Delta\Omega = \Omega_i$), this structure (and possibly other) may be observed at this frequency. These disturbances also appear in figure 14b, between 15 s and 30 s, and then again between 110 s and 130 s, as evidenced by a temporary increase in the height of the mixing layer.

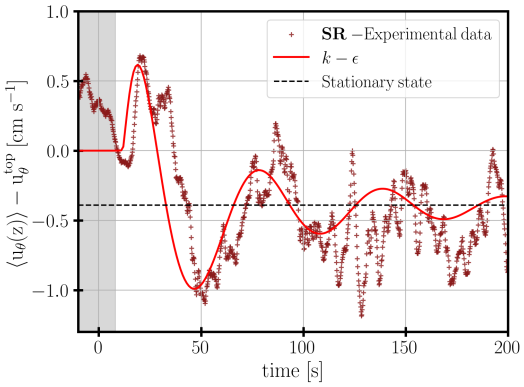

Figure 15. Dots: Temporal evolution of the defect velocity at $z = 3$ cm for EXP-SR. Solid line, same but for the k-ε model. The dashed black line indicates the stationary state after the damping of the oscillations in the k-ε model.

The 1D model reproduces the initial excitation mechanism well: both the amplitude and phase of the first oscillation are captured, aside from a systematic phase shift of approximately 10 s. Agreement deteriorates beyond $t \approx 100$ s, where the experimental signal shows intermittent bursts at a frequency close to f, suggesting that additional processes modulate and phase-shift the inertial response. Most strikingly, while the 1D model predicts a clear monotonic decay, the experimental amplitude does not diminish and even tends to grow with time. This amplification rules out instrumental noise and points to a genuine physical mechanism, possibly a resonance with the inertial frequency.

The value of the drag coefficient $C_f = 5 \times 10^{-3}$ controls the damping rate of the inertial oscillations: a larger C_f would extract momentum more efficiently from the oscillating flow and shorten the decay timescale. The agreement between the experimental data and the 1D model is an independent confirmation of the value of C_f.

5.4.2. *Temporal signature on horizontal transport*

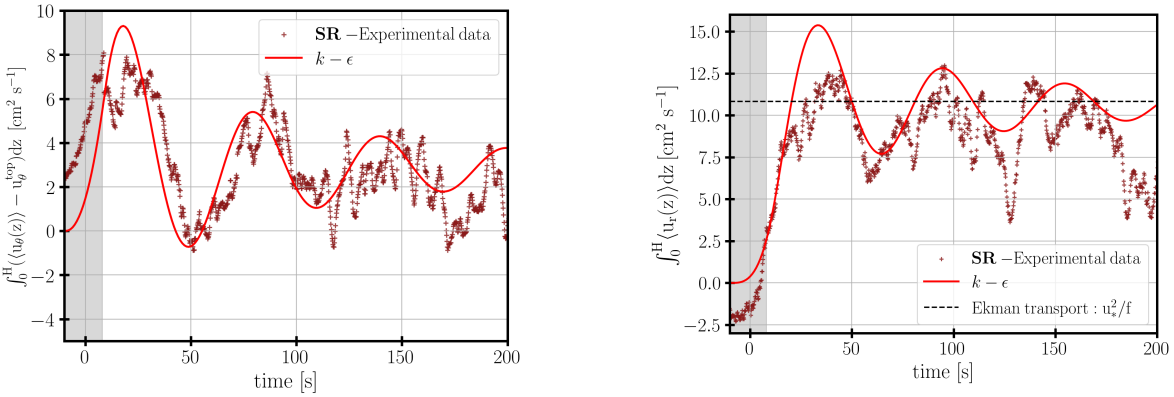

Figure 16. The temporal evolution of the transport between the bottom and $z = 6$ cm for the defect azimuthal velocity (left panel) and for the radial velocity (right panel). In both panel , the solid line show the k-ε model. The dashed black line show the theoretical Ekman transport u_*^2/f.

A more robust evaluation of this transient state can be obtained by considering the vertically integrated transport over the height of the boundary layer (Fig. 16). This height, estimated at 6 cm in Fig. 7 and Fig. 6, remains relatively constant over the first 300 seconds in the case EXP-SR. Figure 16a (resp. 16b) shows the integrated transport between the wall and $z = 6$ cm for the defect azimuthal component (resp. for the radial component).

For the azimuthal defect transport (Figure 16a), the inertial oscillation appears more clearly than at a fixed height. We observe an oscillation close to the frequency f, with a decreasing

amplitude. Once again, there is good agreement with the 1D model in terms of both amplitude and phase, although the same phase shift of the order of 10 s is observed.

The radial transport (Fig. 16b) is more difficult to interpret. Oscillations at the inertial frequency are clearly visible, but other oscillations persist. They appear to be uniform across the full height of the PIV window, rather than confined to the Ekman layer as for the azimuthal component. This contrast is physically meaningful: the azimuthal defect velocity directly reflects the inertial deviation relative to the interior flow, whereas the radial velocity receives significant contributions from non-axisymmetric motions of comparable amplitude, making it more sensitive to large-scale structures that may pre-exist the spin-up.

We can however conclude that the main time scale of the damping is globally well reproduced, even though the experimental envelope remains less regular than in the simulation. The transient response of the flow to an impulsive friction is therefore characterised by the damping of inertial oscillations. This decay controls the duration of the transient regime, the phase relation between radial and azimuthal component and the characteristic time of the steady Ekman layer to be fully developed.

6. Conclusions

In this study, we have investigated the transient dynamics of a fully turbulent Ekman boundary layer through large-scale spin-up experiments conducted on the 13 m Coriolis rotating platform in Grenoble.

An important result is the reliable estimation of the friction velocity in a transient regime through several independent methods: extrapolation of the turbulent momentum flux profile toward the wall, fitting the interior velocity decay to the quadratic friction law (34), and direct comparison with the 1D model. This multi-method approach complements the work of Sous et al. (2013), who estimated the friction velocity under the assumption of a fully established regime, and confirms that $C_b \approx 2.5 \times 10^{-3}$ holds robustly throughout the transient phase.

We also show that unlike the laminar case, where the attenuation rate is set analytically by the viscous Ekman layer, the turbulent experiments show that oscillations persist over several inertial periods, with an amplitude decay slower than predicted by laminar theory. The turbulent experimental case lies between the laminar no-slip and free-slip limits, a behaviour that is directly controlled by the type of bottom stress formulation. We show that the physically consistent representation of the bottom stress in a turbulent regime, where the viscous sublayer is not resolved, is neither a strict no-slip nor a free-slip condition, but rather a quadratic drag law of the form $\tau_b = C_f|\mathbf{u}|\mathbf{u}$, with $C_f \approx 5 \times 10^{-3}$. This formulation, in which the stress depends on the velocity of the fluid relative to the moving boundary, proves essential for correctly reproducing both the damping rate of the inertial oscillations and the spin-up rate of the interior flow. Furthermore, despite the slow attenuation of the oscillations, we verified that the steady Ekman spiral and the transient inertial oscillations superpose linearly to a good approximation, even in the turbulent regime.

The k-ε closure is shown to faithfully reproduce the mean velocity profiles, the turbulent kinetic energy, and the Reynolds stress profiles of the turbulent Ekman layer. In particular, the model correctly captures the vertical confinement of the boundary layer by rotation, the amplitude and phase of the inertial oscillations during the first few periods, and the deepening of the mixed layer in the stratified cases. Estimates of the mixing length derived from the measured turbulent correlations, both with and without background rotation, are consistent with the k-ε scaling.

The k-ε closure relies on the Boussinesq eddy-viscosity hypothesis, which assumes that the Reynolds stress tensor is proportional to the mean strain-rate tensor through a single scalar isotropic eddy viscosity ν_t. In a standard shear-driven boundary layer, this assumption is a

reasonable first approximation, and the k-ε model has been shown to reproduce mean velocity profiles and TKE budgets with acceptable accuracy (Pope 2000). However, in a rotating boundary layer such as the Ekman layer, the Coriolis force introduces a preferred direction that breaks the symmetry between the streamwise and cross-stream components of the Reynolds stress tensor (Svensson 1979). In particular, Direct Numerical Simulations (DNS) studies of the turbulent Ekman layer (Marlatt et al. 2012) have shown that the off-diagonal component $\langle u'v' \rangle$ makes a non-negligible contribution to the turbulent energy budget, a direct consequence of the rotation-induced coupling between the two horizontal velocity components (Wirth 2010). This anisotropy is not captured by the standard k-ε model, which uses a single eddy viscosity for all stress components. More sophisticated closures, such as Reynolds Stress Models (RSM), transport individual components of the Reynolds stress tensor and can, in principle, represent this directional asymmetry (see e.g. Launder et al. 1975). In the present study, the good agreement between the k-ε model and the experimental data suggests that, at the Reynolds numbers considered, the isotropic approximation remains adequate for the mean flow and TKE, even if it may underestimate the cross-stream stress.

The present results have direct implications for the parameterization of oceanic boundary layers in numerical models. In coarse-resolution models, the grid spacing far exceeds the thickness of the turbulent boundary layer, so that the bottom boundary condition is not merely a numerical detail but a physical one with large-scale consequences. The choice of bottom friction parameterization directly controls the energy dissipation rate of the large-scale flow (Gallet and Ferrari 2020, Thompson and Young 2006). This sensitivity underscores the importance of using a physically motivated drag law rather than an ad hoc boundary condition. Imposing a classical no-slip condition directly on the resolved velocity field is inconsistent with the Law of the Wall at coarse resolution: the molecular processes responsible for arresting the flow at the wall are not represented by the eddy-viscosity parameterizations used in such models, and the resulting dissipation is dominated by the artificial shear imposed to meet the no-slip condition (Deremble et al. 2011). Conversely, a free-slip condition sets the tangential stress to zero, which is equally unphysical for a solid boundary. The physically consistent approach is therefore to supplement a free-slip condition with a drag parameterization of the form $\tau_b = C_f |\mathbf{u}| \mathbf{u}$, in the spirit of the Law of the Wall, with $C_f \approx \mathcal{O}(10^{-3})$ as inferred from this study. Future work should extend these results to strongly stratified regimes, where buoyancy limits the vertical penetration of momentum and the interaction between the Ekman layer and the pycnocline becomes the dominant control on mixed-layer deepening.

Acknowledgments

The GOTM model is available at `https://gotm.net/`. The UVMAT software is available at `https://gricad-gitlab.univ-grenoble-alpes.fr/legi/soft/uvmat-doc`

Disclosure statement

The authors report there are no competing interests to declare.

Funding

This research was funded in part by Agence Nationale de la Recherche (ANR), projects ANR-23-CE01-0009 and ANR-15-IDEX-02 and by Initiatives de Recherche à Grenoble Alpes (IRGA) G7H-IRG23D21.

References

Alford, M. H., 2001: Internal Swell Generation: The Spatial Distribution of Energy Flux from the Wind to Mixed Layer Near-Inertial Motions. *Journal of Physical Oceanography*, **31 (8)**, 2359–2368, https://doi.org/10.1175/1520-0485(2001)031⟨2359:ISGTSD⟩2.0.CO;2.

Ashkenazy, Y., H. Gildor, and G. Bel, 2015: The effect of stochastic wind on the infinite depth Ekman layer model. *Europhysics Letters*, **111 (3)**, 39 001, https://doi.org/10.1209/0295-5075/111/39001.

Braun, L., B. A. Younis, and B. Weigand, 2020: A Turbulence Closure Study of the Flow and Thermal Fields in the Ekman Layer. *Boundary-Layer Meteorology*, **175 (1)**, 25–55, https://doi.org/10.1007/s10546-019-00495-8.

Burchard, H., and H. Baumert, 1998: The formation of estuarine turbidity maxima due to density effects in the salt wedge. a hydrodynamic process study. *J. Phys. Oceanogr.*, **28 (2)**, 309–321, https://doi.org/10.1175/1520-0485(1998)028⟨0309:TFOETM⟩2.0.CO;2.

Burchard, H., and K. Bolding, 2001: Comparative Analysis of Four Second-Moment Turbulence Closure Models for the Oceanic Mixed Layer. *Journal of Physical Oceanography*, **31 (8)**, 1943–1968, https://doi.org/10.1175/1520-0485(2001)031⟨1943:CAOFSM⟩2.0.CO;2.

Caldwell, D. R., C. W. Van Atta, and K. N. Helland, 1972: A laboratory study of the turbulent ekman layer. *Geophysical Fluid Dynamics*, **3 (2)**, 125–160, https://doi.org/10.1080/03091927208236078.

Canuto, V. M., A. Howard, Y. Cheng, and M. S. Dubovikov, 2001: Ocean Turbulence. Part I: One-Point Closure Model—Momentum and Heat Vertical Diffusivities. *Journal of Physical Oceanography*, **31 (6)**, 1413–1426, https://doi.org/10.1175/1520-0485(2001)031⟨1413:OTPIOP⟩2.0.CO;2.

Carlsson, B., Y. Papadimitrakis, and A. Rutgersson, 2010: Evaluation of a roughness length model and sea surface properties with data from the baltic sea. *J. Phys. Oceanogr.*, **40 (9)**, 2007–2024, https://doi.org/10.1175/2010JPO4340.1.

Charnock, H., 1955: Wind stress on a water surface. *Quart. J. Roy. Meteor. Soc.*, **81 (350)**, 639–640, https://doi.org/10.1002/qj.49708135027.

Coppin, M., B. Deremble, and J. Sommeria, 2025: Wind-mixed layer deepening in a rotating frame. *Geophysical & Astrophysical Fluid Dynamics*, **119 (5)**, 646–684, https://doi.org/10.1080/03091929.2025.2609460.

Csanady, G., and P. Shaw, 1980: The Evolution of a Turbulent Ekman Layer. *JOURNAL OF GEOPHYSICAL RESEARCH-OCEANS*, **85**, 1537–1547, https://doi.org/10.1029/JC085iC03p01537.

D'Asaro, E. A., 1985: The Energy Flux from the Wind to Near-Inertial Motions in the Surface Mixed Layer. *Journal of Physical Oceanography*, **15**, 1043–1059, https://doi.org/10.1175/1520-0485(1985)015⟨1043:TEFFTW⟩2.0.CO;2.

Deremble, B., A. M. Hogg, P. Berloff, and W. K. Dewar, 2011: On the application of no-slip lateral boundary conditions to 'coarsely' resolved ocean models. *Ocean Model.*, **39 (3-4)**, 411–415, https://doi.org/10.1016/j.ocemod.2011.05.002.

Duck, P. W., and M. R. Foster, 2001: Spin up of homogeneous and stratified fluids. *Annual Review of Fluid Mechanics*, **33**, 231–263, https://doi.org/10.1146/annurev.fluid.33.1.231.

Ekman, V. W., 1905: On the influence of the earth's rotation on ocean-currents. *Arkiv för Matematik,, Astronomy Och Fysik*, **2,**, 1–53.

Endoh, M., and T. Nitta, 1971: A Theory of Non-Stationary Oceanic Ekman Layer. *Journal of the Meteorological Society of Japan. Ser. II*, **49 (4)**, 261–266, https://doi.org/10.2151/jmsj1965.49.4_261.

Faller, A. J., and R. Kaylor, 1966: Oscillatory and transitory Ekman boundary layers. Tech. Rep. BN-461.

Fernando, H. J. S., 1991: Turbulen mixing in stratified fluids. *Annual Review of Fluid Mechanics*, **23**, 455–493, https://doi.org/10.1146/annurev.fl.23.010191.002323.

Gallet, B., and R. Ferrari, 2020: The vortex gas scaling regime of baroclinic turbulence. *Proc. Natl. Acad. Sci. U.S.A.*, **117 (9)**, 4491–4497, https://doi.org/10.1073/pnas.1916272117.

Garratt, J. R., 1992: *The atmospheric boundary layer*. New York, NY (United States); Cambridge University Press.

Greenspan, H. P., and L. N. Howard, 1963: On a time-dependent motion of a rotating fluid. *Journal of Fluid Mechanics*, **17 (3)**, 385–404, https://doi.org/10.1017/S0022112063001415.

Howard, L. N., 1961: Note on a paper of john w. miles. *J. Fluid Mech.*, **10 (4)**, 509–512, https://doi.org/10.1017/S0022112061000317.

Imayama, S., R. J. Lingwood, and P. H. Alfredsson, 2014: The turbulent rotating-disk boundary layer. *European Journal of Mechanics-B/Fluids*, **48**, 245–253.

Kato, H., and O. M. Phillips, 1969: On the penetration of a turbulent layer into stratified fluid. *Journal of Fluid Mechanics*, **37**, 643–655, https://doi.org/10.1017/S0022112069000784.

Kim, S. Y., P. M. Kosro, and A. L. Kurapov, 2014: Evaluation of directly wind-coherent near-inertial surface currents off Oregon using a statistical parameterization and analytical and numerical models. *Journal of Geophysical Research: Oceans*, **119 (10)**, 6631–6654, https://doi.org/10.1002/2014JC010115.

Kozul, M., D. Chung, and J. Monty, 2016: Direct numerical simulation of the incompressible temporally developing turbulent boundary layer. *Journal of Fluid Mechanics*, **796**, 437–472.

Launder, B. E., G. J. Reece, and W. Rodi, 1975: Progress in the development of a reynolds-stress turbulence closure. *J. Fluid Mech.*, **68 (3)**, 537–566, https://doi.org/10.1017/S0022112075001814.

Lewis, D. M., and S. E. Belcher, 2004: Time-dependent, coupled, Ekman boundary layer solutions incorporating Stokes drift. *Dynamics of Atmospheres and Oceans*, **37 (4)**, 313–351, https://doi.org/10.1016/j.dynatmoce.

2003.11.001.

Lingwood, R. J., 1996: An experimental study of absolute instability of the rotating-disk boundary-layer flow. *Journal of Fluid Mechanics*, **314**, 373–405, https://doi.org/10.1017/S0022112096000365.

Madsen, O. S., 1977: A Realistic Model of the Wind-Induced Ekman Boundary Layer. *Journal of Physical Oceanography*, **7 (2)**, 248–255, https://doi.org/10.1175/1520-0485(1977)007⟨0248:ARMOTW⟩2.0.CO;2.

Marlatt, S., S. Waggy, and S. Biringen, 2012: Direct Numerical Simulation of the Turbulent Ekman Layer: Evaluation of Closure Models. *Journal of the Atmospheric Sciences*, **69 (3)**, 1106–1117, https://doi.org/10.1175/JAS-D-11-0107.1.

McPhaden, M. J., K. Athulya, M. S. Girishkumar, and M. Orlić, 2024: Ekman revisited: Surface currents to the left of the winds in the northern hemisphere. *Sci. Adv.*, **10 (46)**, https://doi.org/10.1126/sciadv.adr0282.

Miles, J. W., 1961: On the stability of heterogeneous shear flows. *J. Fluid Mech.*, **10 (4)**, 496–508, https://doi.org/10.1017/S0022112061000305.

Pedlosky, J., 1996: *Ocean Circulation Theory*. Springer, https://doi.org/10.1007/978-3-662-03204-6.

Perlin, A., J. N. Moum, J. M. Klymak, M. D. Levine, T. Boyd, and P. M. Kosro, 2005: A modified law-of-the-wall applied to oceanic bottom boundary layers. *J. Geophys. Res. Oceans*, **110 (C10)**, https://doi.org/10.1029/2004JC002310.

Perlin, A., J. N. Moum, J. M. Klymak, M. D. Levine, T. Boyd, and P. M. Kosro, 2007: Organization of stratification, turbulence, and veering in bottom ekman layers. *J. Geophys. Res. Oceans*, **112 (C5)**, https://doi.org/10.1029/2004JC002641.

Pollard, R., and R. Millard, 1970: Comparison between observed and simulated wind-generated inertial oscillations. *Deep Sea Research and Oceanographic Abstracts*, **17 (4)**, 813–821, https://doi.org/10.1016/0011-7471(70)90043-4.

Pollard, R. T., P. B. Rhines, and R. Thompson, 1973: The deepening of the wind-Mixed layer. *Geophysical Fluid Dynamics*, https://doi.org/10.1080/03091927208236105.

Pope, S. B., 2000: *Turbulent Flows*. Cambridge University Press.

Price, J. F., C. N. K. Mooers, and J. C. Van Leer, 1978: Observation and simulation of storm-induced mixed-layer deepening. *J. Phys. Oceanogr.*, **8 (4)**, 582–599, https://doi.org/10.1175/1520-0485(1978)008⟨0582:OASOSI⟩2.0.CO;2.

Price, J. F., R. A. Weller, and R. Pinkel, 1986: Diurnal cycling: Observations and models of the upper ocean response to diurnal heating, cooling, and wind mixing. *J. Geophys. Res.*, **91**, 8411–8427, https://doi.org/10.1029/JC091iC07p08411.

Rodi, W., 1987: Examples of calculation methods for flow and mixing in stratified fluids. *Journal of Geophysical Research: Oceans*, **92 (C5)**, 5305–5328, https://doi.org/10.1029/JC092iC05p05305.

Rossby, C.-G., and R. B. Montgomery, 1935: The layer of frictional influence in wind and ocean currents. https://doi.org/10.1575/1912/1157.

Sous, D., J. Sommeria, and D. Boyer, 2013: Friction law and turbulent properties in a laboratory Ekman boundary layer. *Physics of Fluids*, **25 (4)**, 046 602, https://doi.org/10.1063/1.4802045.

Speziale, C. G., R. Abid, and E. C. Anderson, 1992: Critical evaluation of two-equation models for near-wall turbulence. *AIAA journal*, **30 (2)**, 324–331.

Svensson, U., 1979: Structure of the Turbulent Ekman Layer. *TELLUS*, **31 (4)**, 340–350.

Thompson, A. F., and W. R. Young, 2006: Scaling baroclinic eddy fluxes: Vortices and energy balance. *J. Phys. Oceanogr.*, **36 (4)**, 720–738, https://doi.org/10.1175/JPO2874.1.

Umlauf, L., and H. Burchard, 2003: A generic length-scale equation for geophysical turbulence models. *Journal of Marine Research*, **61(2)**, 235–265, https://doi.org/10.1357/002224003322005087.

Umlauf, L., and H. Burchard, 2005: Second-order turbulence closure models for geophysical boundary layers. a review of recent work. *Continental Shelf Research*, **25 (7-8)**, 795–827.

Vallis, G., 2006: *Atmospheric and Oceanic Fluid Dynamics*. https://doi.org/10.2277/0521849691.

Weatherly, G. L., and P. J. Martin, 1978: On the structure and dynamics of the oceanic bottom boundary layer. *J. Phys. Oceanogr.*, **8 (4)**, 557–570, https://doi.org/10.1175/1520-0485(1978)008⟨0557:OTSADO⟩2.0.CO;2.

Wirth, A., 2010: On the Ekman Spiral with an Anisotropic Eddy Viscosity. *Boundary-Layer Meteorology*, **137 (2)**, 327–331, https://doi.org/10.1007/s10546-010-9527-7.

Wunsch, C., and R. Ferrari, 2004: Vertical mixing, energy, and the general circulation of the oceans. *Annu. Rev. Fluid Mech.*, **36**, 281–314, https://doi.org/10.1146/annurev.fluid.36.050802.122121.

Zilitinkevich, S., and D. V. Mironov, 1996: A multi-limit formulation for the equilibrium depth of a stably stratified boundary layer. *Boundary-Layer Meteorology*, **81 (3)**, 325–351, https://doi.org/10.1007/BF02430334.

Zilitinkevich, S. S., 2012: The Height of the Atmospheric Planetary Boundary layer: State of the Art and New Development. *National Security and Human Health Implications of Climate Change*, H. J. S. Fernando, Z. Klaić, and J. McCulley, Eds., Springer Netherlands, Dordrecht, 147–161, https://doi.org/10.1007/978-94-007-2430-3_13.

Appendix A: Statistics of the mean and the turbulent fluctuation field

We consider the 2D $(x-z)$ vertical-plane of the laser sheet, which is perpendicular to the radius at its middle section.

The instantaneous velocity field is of dimension $u(x,z,t)$. The average mean flow is obtained with a spatial average (over $N_x = 321$ grid points in the $x-$axis) and a temporal average (3 s, which corresponds to $N_t = 15$ snapshots)

$$\langle u(z,t)\rangle = \int_{x_{min}}^{x_{max}} \int_{t-1.5s}^{t+1.5s} u(z,t)\ dt\ dx.$$

This spatio-temporal average represents the mean flow over $N_x \times N_t = 4815$ profiles.

The turbulent fluctuations are obtained by subtraction, for each time t_i and each $x-$position x_i, the instantaneous velocity field by the spatio-temporal average

$$u'(x_i,z,t_i) = u\ (x_i,z,t_i) - \langle u(z,t_i)\rangle$$

And finally the cross correlation are averaged following the same method than for the mean flow but for a temporal neighbourhood of 10 s ($N_t = 50$ snapshots).

$$\langle\, u'w'(z,t)\,\rangle = \int_{t-5s}^{t+5s} \int_{x_{min}}^{x_{max}} (u\ (x_i,z,t_i) - \langle u(z,t_i)\rangle) \times (w\ (x_i,z,t_i) - \langle w(z,t_i)\rangle)\ dx\,dt \quad \text{(A.1)}$$

Appendix B: Single-column model setting: k-ε closure

We use the open-source GOTM model (General Ocean Turbulence Model) in the single column configuration to numerically solve Equations (12). This model solves the momentum, salt and heat transport equations in a 1D water column, using the k-ε model of turbulence. In this model, the eddy viscosity ν_t and eddy diffusivity of buoyancy ν'_t are locally expressed from the turbulent kinetic energy (TKE) k and the TKE dissipation rate ε as

$$\nu_t = c_\mu \frac{k^2}{\varepsilon} \qquad \nu'_t = c'_\mu \frac{k^2}{\varepsilon}\,. \quad \text{(B.1)}$$

The coefficients c_μ and c'_μ depend on the local stratification and vertical shear. We use Canuto et al. (2001)'s formulation corresponding to the case denoted 'CA' by Burchard and Bolding (2001), and 'CHCD01A' by Umlauf and Burchard (2005). However the stratification effects remain small in our study, so the coefficients c_μ and c'_μ remain close to the value 0.09 classically used in shear flows with uniform density.

The equation for the TKE $k \equiv \overline{\mathbf{u}'^2}/2$ is written as a transport equation

$$\frac{\partial k}{\partial t} + \frac{\partial T_k}{\partial z} = P + B - \varepsilon \quad \text{(B.2)}$$

involving an eddy flux T_k, a production rate P, a conversion rate to potential energy B, and the dissipation rate ε. The eddy flux is modelled by a diffusion law $T_k = -\nu_t \partial k/\partial z$, while P and B can be exactly expressed from the correlations of turbulent fluctuations.

The production P is set by the shear according to

$$P = -\overline{u'w'}\frac{\partial u}{\partial z} - \overline{v'w'}\frac{\partial v}{\partial z} = \nu_t \left|\frac{\partial \mathbf{u}}{\partial z}\right|^2 \quad \text{(B.3)}$$

(the notation $\bar{\cdot}$ and $\cdot'$ denote the standard ensemble averaging and deviation from the ensemble mean respectively).

The conversion rate to potential energy B also represents the vertical flux of buoyancy. Within the eddy diffusivity hypothesis, it is expressed as

$$B = \overline{w'b'} = -\nu_t' \frac{\partial b}{\partial z} \equiv -\nu_t' N^2 \,, \tag{B.4}$$

introducing the local buoyancy frequency $N(z,t)$.

A transport equation with similar form is empirically introduced for ε to close the system,

$$\frac{\partial \varepsilon}{\partial t} + \frac{\partial}{\partial z}\left(\frac{\nu_t}{\sigma_\varepsilon}\frac{\partial \varepsilon}{\partial z}\right) = \frac{\varepsilon}{k}\left(c_{\varepsilon 1}\, P + c_{\varepsilon 3}\, \overline{w'b'} - c_{\varepsilon 2}\, \varepsilon\right) . \tag{B.5}$$

We use the classical values $\sigma_\varepsilon = 1.3$, $c_{\varepsilon 1} = 1.44$, and $c_{\varepsilon 2} = 1.92$ (Rodi 1987). The parameter $c_{\varepsilon 3}$ is less consensual, but it is of weak relevance in our case of weak stratification. We use here $c_{\varepsilon 3} = -0.621$ (Burchard and Bolding 2001).

The boundary condition at $z = 0$ is a key difficulty. At the air-sea interface, the boundary condition is generally set as a given wind stress u_*^2 at the free surface. By contrast the wall velocity is imposed in our experiments, a common situation in the engineering context. Then the turbulent region must be matched with the viscous sub-layer, which requires appropriate modification of the k-ε or the related k-ω model (Speziale et al. 1992).

We here use a simplified approach by considering that our first grid point, at $z = z_1$ is in a log layer. This log-layer is characterized by a constant shear stress u_*^2 with an angle α_0 with respect to the azimuthal direction. In this log layer, the fluid is well mixed, so that $B = 0$ in Eq. (B.2), and the TKE production locally balances dissipation. Considering that $\nu_t = \kappa u_* z$ (where $\kappa \simeq 0.41$ is the von Karman constant), we get for $z \to 0$,

$$\kappa z \frac{\partial u}{\partial z} \to u_* \sin\alpha_0 \tag{B.6a}$$

$$\kappa z \frac{\partial v}{\partial z} \to u_* \cos\alpha_0 \tag{B.6b}$$

$$k = c_\mu^{-1/2} u_*^2 \tag{B.6c}$$

$$\varepsilon = P = u_*^3/(\kappa z) \tag{B.6d}$$

This provides an appropriate set of boundary conditions for the k-ε equations if the wall stress is imposed. The velocity then diverges logarithmically,

$$u(z) = \frac{u_*}{\kappa}\sin\alpha_0 \ \ln\!\left(\frac{z}{z_0}\right) \tag{B.7a}$$

$$v(z) - v_0 = \frac{u_*}{\kappa}\cos\alpha_0 \ \ln\!\left(\frac{z}{z_0}\right) \tag{B.7b}$$

In the case of a smooth wall, the expression $u/u_* = \kappa^{-1}\ln(z u_*/\nu) + 5.2$ is generally used instead (see for instance Pope 2000). This is recovered from (B.7) with the expression $z_0 \simeq (\nu/u_*)\ \exp(-5.2\ \kappa) \simeq\ 0.12\ \nu/u_*$.

Let us assume that the first grid point z_1 is in the log layer, so that $z_1 \gg z_0$. There is a velocity shift $\mathbf{u}(z_1) - \mathbf{u_b}$ with respect to the boundary velocity $\mathbf{u_b}$ which is aligned with the shear stress. The square of modulus of this velocity shift is proportional to the shear stress u_*^2,

$$u_*^2 = C_f |\mathbf{u}(z_1) - \mathbf{u_{wall}}|^2 \tag{B.8}$$

where $C_f = [\kappa/\ln(z_1/z_0)]^2$ according to Eq. (B.7). This coefficient depends only logarithmically on the shear stress u_* and the grid mesh z_1. In our calculations $z_1 = 0.1$ cm and u_*

remains of the order of 1 cm s^{-1}, leading to $C_f = 8.6 \times 10^{-3}$. The value of C_f obtained here is somewhat greater than the reference value of 5×10^{-3} found in this study. This discrepancy may be attributed to the moderate Reynolds number of the present experiments, for which the turbulent boundary layer is not yet fully developed and the logarithmic layer is not firmly established. We find that the results are not sensitive to this choice, thanks to the logarithmic dependency.

The roughness length z_0 depends strongly on the surface type and flow regime. For a smooth wall, the viscous scaling $z_0 \simeq 0.12\,\nu/u_*$ applies, giving $z_0 \sim \mathcal{O}(10^{-5})$ m for typical oceanic friction velocities. In the ocean, the situation is more complex. At the sea surface, the wind-roughened interface introduces an aerodynamic roughness; under moderate winds and in the absence of surface waves, values of $z_0 \approx 0.02$ m are commonly reported (e.g. Charnock 1955), and wave breaking can significantly enhance z_0 above this baseline (Carlsson et al. 2010). At the seafloor, the roughness is set by sediment grain size and bedform geometry, and is on the order of $z_0 \sim 10^{-3} - 10^{-4}$ m (Weatherly and Martin 1978). Through the expression $C_f = [\kappa/\ln(z_1/z_0)]^2$, this spread of z_0 values translates into a relatively modest uncertainty in C_f, owing to the logarithmic dependence, consistent with the range $C_f \sim \mathcal{O}(10^{-3})$ inferred from the present study.

Equations (B.8) and (B.6c-d) can be used in principle to solve the k-ε equations. However, it has been shown by Burchard and Baumert (1998) that Neumann conditions are numerically more stable. These follow directly by differentiating Eqs. (B.6c-d) with respect to z:

$$\frac{\partial k}{\partial z} = 0, \tag{B.9a}$$

$$\frac{\partial \varepsilon}{\partial z} = -\frac{u_*^3}{\kappa (z_1)^2}\,. \tag{B.9b}$$

The no-flux condition is also used for the temperature.

The simulations are configured to match the laboratory experiments at radius $r_0 = 4.5$ m (the PIV measurement location). The vertical grid spacing is 0.1 cm over a domain extending 50 cm along the z-axis. Simulations run for 600 s with a time step of 0.1 s. The surface stress is imposed as a linear ramp rather than an impulsive condition, in order to reproduce the finite spin-up time of the rotating platform. The origin $t = 0$ is defined as the midpoint of the ramp, where the velocity reaches half its nominal value. We set the Coriolis parameter to $f = 0.1$ s^{-1}, corresponding to the initial rotation rate of the laboratory experiments, and set $f = 0$ in the non-rotating cases. The initial temperature profile used in the 1D simulations are interpolated on the vertical grid of the model from experimental measurement.

Appendix C: Calibration of the Drag coefficient for the 1D model

The drag coefficient C_f is calibrated by matching the steady-state cross-isobaric angle α_0 predicted by the k-ε model to the DNS reference value of Marlatt et al. (2012). Simulations are run in Cartesian geometry (without centrifugal acceleration terms) to reproduce the planar configuration of the DNS, and are integrated until inertial oscillations are fully damped so that α_0 reflects only the mean boundary-layer structure. Figure C1 shows α_0 as a function of C_f for two vertical grid resolutions. For the fine grid ($z_1 = 0.1$ cm), the DNS reference value $\alpha_0^{\mathrm{DNS}} = 18.56^\circ$ is matched at $C_f \approx 5 \times 10^{-3}$, which is therefore adopted in all k-ε simulations presented in this study. The coarse grid ($z_1 = 0.5$ cm) systematically overestimates α_0 regardless of C_f, confirming that adequate near-wall resolution is required for a reliable calibration.

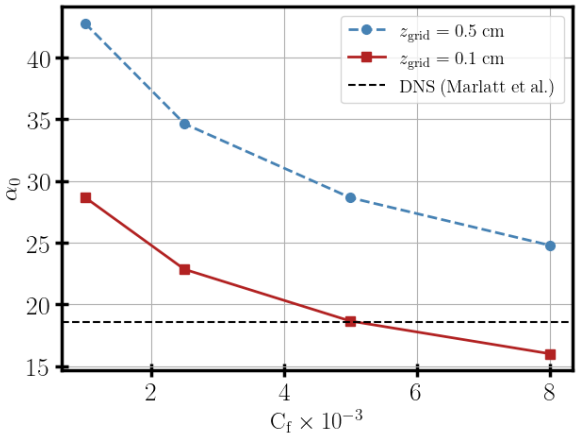

Figure C1. Cross-isobar angle measured a the first grid point as a function of the bottom drag coefficient C_f, computed at steady state (inertial oscillation are fully damped) for two vertical grid resolutions: $z_1 = 0.5$ cm (circles, dashed) and $z_1 = 0.1$ cm (squares, solid). Horizontal lines indicate the DNS reference values of reported by Marlatt et al. (2012) (18.56, dashed) for a steady Ekman layer at $Re = 1000$. Centrifugal acceleration terms are excluded from all simulation shown

Appendix D: Assessment of the single-column approximation

The validity of the single-column framework for axisymmetric geometry, particularly when the Rossby number $Ro \approx 1$, is based on the assumption that the vertical momentum advection terms, associated with Ekman pumping, remain small compared to the centrifugal acceleration terms retained in the model. In order to evaluate this assumption, we compare, based on experimental data (EXP-REF and EXP-SR) at a given height $z = 4$ cm, the amplitudes of the various non-linear terms appearing in equations (12)b and (12)c (Figures D1 and D2).

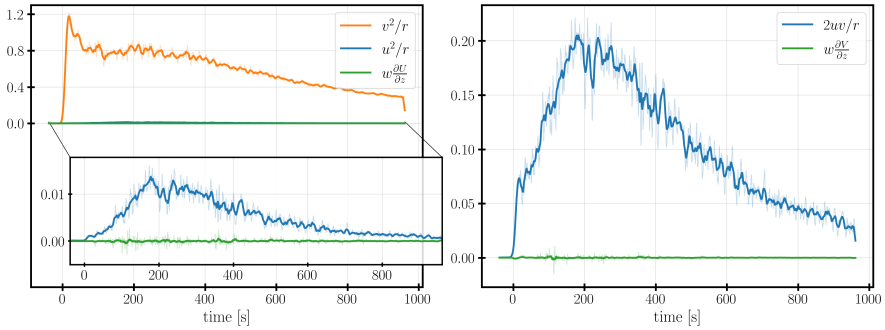

Figure D1. Time series of the non-linear terms entering Eq. 12, evaluated from the experimental data (EXP-REF) at $z = 4$ cm. Left: radial momentum equation (v^2/r_0, u^2/r_0, and $w\,\partial u/\partial z$). Right: azimuthal momentum equation ($2uv/r_0$ and $w\,\partial v/\partial z$). The inset in the left panel highlights the weaker contributions u^2/r_0 and $w\,\partial u/\partial z$.

In the non-rotating case (EXP-REF), the vertical advection term $w\partial u/\partial z$ is negligible compared to the dominant contribution v^2/r_0, which is several orders of magnitude larger (see the inset in Fig. D1). The contribution u^2/r_0, although weaker than v^2/r_0, remains significantly greater than the vertical advection. The same observation applies to the azimuthal equation, where $w\partial v/\partial z$ remains much smaller than $2uv/r_0$

The presence of rotation does not modify this scaling, the vertical advective terms $w\partial u/\partial z$ and $w\partial v/\partial z$ are still several order weaker than the dominant terms v^2/r_0 and the Coriolis terms (fv, fu). Nevertheless, it should be noted that u^2/r_0 and $w\partial u/\partial z$ become comparable in amplitude here, but in order to maintain consistency with the cases modelled without rotation, we have chosen to retain all the centrifugal acceleration terms in the cases involving initial rotation

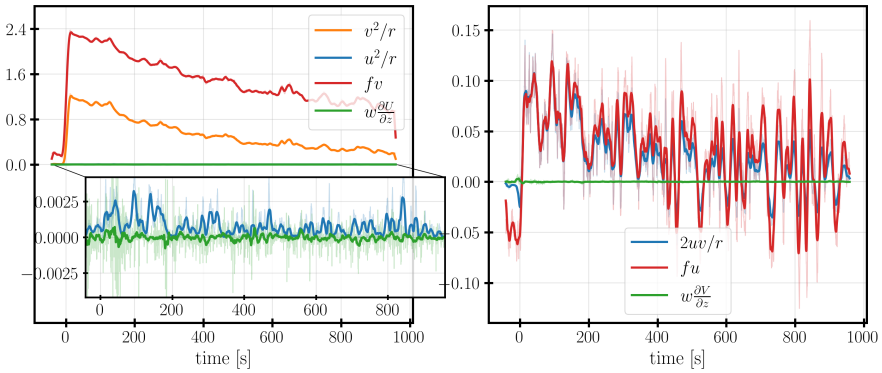

Figure D2. Same as Fig. D1 but for case SR